Calhoun: The NPS Institutional Archive

DSpace Repository

Theses and Dissertations | 1. Thesis and Dissertation Collection, all items

2013-06

Characterization of residual stress as a function of friction stir welding parameters in ODS steel MA956

Bennett, Martin S.

Monterey, California: Naval Postgraduate School

http://hdl.handle.net/10945/34627

This publication is a work of the U.S. Government as defined in Title 17, United States Code, Section 101. Copyright protection is not available for this work in the United States.

Downloaded from NPS Archive: Calhoun

http://www.nps.edu/library

Calhoun is the Naval Postgraduate School's public access digital repository for research materials and institutional publications created by the NPS community. Calhoun is named for Professor of Mathematics Guy K. Calhoun, NPS's first appointed -- and published -- scholarly author.

Dudley Knox Library / Naval Postgraduate School
411 Dyer Road / 1 University Circle
Monterey, California USA 93943

NAVAL POSTGRADUATE SCHOOL

MONTEREY, CALIFORNIA

THESIS

CHARACTERIZATION OF RESIDUAL STRESS AS A FUNCTION OF FRICTION STIR WELDING PARAMETERS IN ODS STEEL MA956

by

Martin S. Bennett

June 2013

Thesis Advisor:	Luke N. Brewer
Second Reader:	Sarath K. Menon

Approved for public release; distribution is unlimited

THIS PAGE INTENTIONALLY LEFT BLANK

REPORT DOCUMENTATION PAGE			Form Approved OMB No. 0704–0188
Public reporting burden for this collection of information is estimated to average 1 hour per response, including the time for reviewing instruction, searching existing data sources, gathering and maintaining the data needed, and completing and reviewing the collection of information. Send comments regarding this burden estimate or any other aspect of this collection of information, including suggestions for reducing this burden, to Washington headquarters Services, Directorate for Information Operations and Reports, 1215 Jefferson Davis Highway, Suite 1204, Arlington, VA 22202–4302, and to the Office of Management and Budget, Paperwork Reduction Project (0704–0188) Washington DC 20503.			
1. AGENCY USE ONLY *(Leave blank)*	**2. REPORT DATE** June 2013	**3. REPORT TYPE AND DATES COVERED** Master's Thesis	
4. TITLE AND SUBTITLE CHARACTERIZATION OF RESIDUAL STRESS AS A FUNCTION OF FRICTION STIR WELDING PARAMETERS IN ODS STEEL MA956			**5. FUNDING NUMBERS**
6. AUTHOR(S) Martin S. Bennett			
7. PERFORMING ORGANIZATION NAME(S) AND ADDRESS(ES) Naval Postgraduate School Monterey, CA 93943–5000			**8. PERFORMING ORGANIZATION REPORT NUMBER**
9. SPONSORING /MONITORING AGENCY NAME(S) AND ADDRESS(ES) N/A			**10. SPONSORING/MONITORING AGENCY REPORT NUMBER**
11. SUPPLEMENTARY NOTES The views expressed in this thesis are those of the author and do not reflect the official policy or position of the Department of Defense or the U.S. Government. IRB Protocol number ____N/A____.			
12a. DISTRIBUTION / AVAILABILITY STATEMENT Approved for public release; distribution is unlimited			**12b. DISTRIBUTION CODE**

13. ABSTRACT

This thesis characterizes the residual stresses generated by friction stir welding of ODS steel MA956 as a function of heat index. The heat index of a weld is used to determine relative heat input among different friction stir welding conditions. It depends on a combination of the rotational speed and traverse, or welding speed of the tool through the metal. Higher rotational speeds and lower traverse speeds increase heat index and are expected to result in lower residual stresses than welds performed with lower heat index. Three conditions with varying heat indices were selected from high to low: 500 rpm/25 millileters per minute (mmpm), 400 rpm/50 mmpm and 400 rpm/100 mmpm. The full stress tensor was determined for points across these welds using x-ray diffraction. Longitudinal residual stresses approximately 90% of yield strength were observed for the lowest heat input condition. Stress profiles displayed the characteristic "M" shaped profile, and asymmetry between advancing and retreating stress peaks was limited, occurring mainly on the root of the weld. As expected, lowering the heat index of a weld increased the magnitude of residual stresses across the whole weld profile.

14. SUBJECT TERMS Friction stir welding, residual stress, heat input, ODS steel, MA956			**15. NUMBER OF PAGES** 67
			16. PRICE CODE
17. SECURITY CLASSIFICATION OF REPORT Unclassified	**18. SECURITY CLASSIFICATION OF THIS PAGE** Unclassified	**19. SECURITY CLASSIFICATION OF ABSTRACT** Unclassified	**20. LIMITATION OF ABSTRACT** UU

NSN 7540–01–280–5500 Standard Form 298 (Rev. 2–89)
Prescribed by ANSI Std. 239–18

THIS PAGE INTENTIONALLY LEFT BLANK

Approved for public release; distribution is unlimited

CHARACTERIZATION OF RESIDUAL STRESS AS A FUNCTION OF FRICTION STIR WELDING PARAMETERS IN ODS STEEL MA956

Martin S. Bennett
Ensign, United States Navy
B.S., United States Naval Academy 2012

Submitted in partial fulfillment of the
requirements for the degree of

MASTER OF SCIENCE IN MECHANICAL ENGINEERING

from the

NAVAL POSTGRADUATE SCHOOL
June 2013

Author: Martin S. Bennett

Approved by: Luke N. Brewer
Thesis Advisor

Sarath K. Menon
Second Reader

Knox T. Millsaps
Chair, Department of Mechanical and Aerospace Engineering

THIS PAGE INTENTIONALLY LEFT BLANK

ABSTRACT

This thesis characterizes the residual stresses generated by friction stir welding of ODS steel MA956 as a function of heat index. The heat index of a weld is used to determine relative heat input among different friction stir welding conditions. It depends on a combination of the rotational speed and traverse, or welding speed of the tool through the metal. Higher rotational speeds and lower traverse speeds increase heat index and are expected to result in lower residual stresses than welds performed with lower heat index. Three conditions with varying heat indices were selected from high to low: 500 rpm/25 millileters per minute (mmpm), 400 rpm/50 mmpm and 400 rpm/100 mmpm. The full stress tensor was determined for points across these welds using x-ray diffraction. Longitudinal residual stresses approximately 90% of yield strength were observed for the lowest heat input condition. Stress profiles displayed the characteristic “M” shaped profile, and asymmetry between advancing and retreating stress peaks was limited, occurring mainly on the root of the weld. As expected, lowering the heat index of a weld increased the magnitude of residual stresses across the whole weld profile.

THIS PAGE INTENTIONALLY LEFT BLANK

TABLE OF CONTENTS

I. INTRODUCTION....1
- **A. BACKGROUND....1**
- **B. X-RAY DIFFRACTION FOR MEASUREMENT OF RESIDUAL STRESS....11**
- **C. THESIS OBJECTIVES....20**

II. EXPERIMENTAL METHODS....21
- **A. MA956 SPECIFICATIONS AND WELDING PARAMETERS....21**
- **B. X-RAY DIFFRACTION....21**

III. EXPERIMENTAL RESULTS....29
- **A. RESIDUAL STRESS PROFILES....29**
- **B. RESIDUAL STRESSES AS A FUNCTION OF DEPTH FROM THE SURFACE....33**

IV. DISCUSSION....37
- **A. RESIDUAL STRESS PROFILES....37**
- **B. IMPLICATIONS....41**

V. CONCLUSIONS....45

LIST OF REFERENCES....47

INITIAL DISTRIBUTION LIST....49

THIS PAGE INTENTIONALLY LEFT BLANK

LIST OF FIGURES

Figure 1. Temperature ranges for various structural materials subjected to intermediate doses. The operating temperature is usually limited by thermal creep on the high side and radiation embrittlement on the low side. From Zinkle [2] 1

Figure 2. (a) A schematic of the FSW process. From Mishra [13]. The cross section from a FSW plate (b). From [5]. 4

Figure 3. Engineering stress/strain curves for FSW MA956 at room temperature (a) and 600°C (b) From Baker [5] 6

Figure 4. A simplified example of residual stresses developed during welding. The red region represents the size of the heated region upon cooling in the absence of constraint. The bold region represents the actual area the cooled metal will occupy in the presence of tensile residual stresses. The actual heated region has many more sub-regions with different cooling rates, and the mismatch in their contraction will result in residual stresses. 8

Figure 5. (a) Residual stress profiles for the FSW of AA 5083. From Peel [15]. (b) The residual stress profile across PM2000, an ODS steel nearly identical to MA956. From Mathon [20]. 10

Figure 6. A diagram showing diffraction occurring according to Bragg's Law. From [21] 12

Figure 7. A diagram of different planar spacing due to residual stress. Ψ angles are normal to the measured plane. In this experiment {211} planes were used [22]. 13

Figure 8. Peak shifts in low stress (a) and high stress (b) samples at $\psi = 3.09°$ and 36.84°. While (b) was stressed to -502 MPa, the diffraction peak shift is small. This shows how even small lattice strains can produce large stresses. 14

Figure 9. Sample geometry for this experiment [22]. 15

Figure 10. A d vs. $\sin^2\psi$ plot for a stress free ferritic steel powder (a) and a high stress ferritic steel standard (-502 MPa) (b) 17

Figure 11. Calculated penetration of Cr x-rays into MA956. 19

Figure 12. Proto Manufacturing's iXRD. Samples are measured under the head on the left side of the instrument (a). A close-up of the goniometer and the position sensitive scintillation detectors is given in (b). Chromium x-rays traveling through the collimator irradiate the sample. Left and right detectors are arranged to collect the diffracted beams. 22

Figure 13. The two plates used in this analysis. The wider plate (a), will be referred to as Plate 1, while the narrow plate in (b) will be referred to as Plate 2. Scan locations and direction are shown as well as the locations of the advancing and retreating sides of the weld, which are consistent from Plate 1 to Plate 2 25

Figure 14. Proto Manufacturing's Electropolisher (a) and the position for stress at depth measurements (b) 27

Figure 15. Longitudinal stress from the crown of Plate 1. 29
Figure 16. Longitudinal residual stress maximum values in the crown of Plate 1, on the advancing side (negative values for position always indicate advancing side of the weld nugget). 30
Figure 17. Longitudinal stress profile from the crown of Plate 2. 31
Figure 18. Transverse stress from the crown of Plate 1 32
Figure 19. Out of plane stress for the 500/25 condition in Plate 1 32
Figure 20. Residual stress tensors for 500/25 BM (a), 500/25 SZ (B), 400/50 SZ (c) and 400/100 SZ (d). All stresses reported in MPa. Tensors are symmetric.....33
Figure 21. Longitudinal stress with depth measurements for the 400/100 condition 34
Figure 22. (a)Stress tensor values for the SZ of the 400/100 condition. (b) Stress tensor values for the TMAZ of the 400/100 condition. All stresses given in MPa. The tensor is symmetric. 34
Figure 23. Residual stress profiles from the root of the weld on Plate 1 35
Figure 24. Normalized Longitudinal stresses from the crown of Plate 1. Data within 10 mm of the weld centerline was normalized to a yield strength of 530 MPa or 539 MPa (500/25 and 400/100, respectively), while data beyond these points were normalized to the BM yield of 909 MPa. 39
Figure 25. A Modified-Goodman plot for the stir zone of the 400/100 condition. The measured residual stresses are near the yield strength of the SZ. In this example, for a safety factor of 1 (failure), an alternating load of only 89 MPa need be applied. 42

LIST OF TABLES

Table 1. Chemical composition of MA956. From [5] 21
Table 2. Triaxial stress measurements conditions used for measurements in Plate 1 and Plate 2 (MET scans on unstressed powder and high stress standard were taken with ϕ=0° only) 23
Table 3. Sample MET scans performed for instrument alignment 24
Table 4. Depth measurements after electropolishing 26

THIS PAGE INTENTIONALLY LEFT BLANK

LIST OF ACRONYMS AND ABBREVIATIONS

ODS	Oxide Dispersion Strengthened
FSW	Friction Stir Welding
HI	Heat Index
SZ	Stir Zone
TMAZ	Thermo Mechanically Affected Zone
HAZ	Heat Affected Zone
BM	Base Metal
RPM	Revolutions per Minute
MMPM	Millimeters per Minute

THIS PAGE INTENTIONALLY LEFT BLANK

ACKNOWLEDGMENTS

I would like to acknowledge the hard work and mentorship of Professors Luke Brewer and Sarath Menon. Without their guidance and patience, this project would not have been possible. Also, I would like to thank Lawrence Livermore National Laboratory for providing funding and the scarce MA956 plate for research and Murray Mahoney of MegaStir for performing friction stir welding on the MA956 plate.

THIS PAGE INTENTIONALLY LEFT BLANK

I. INTRODUCTION

A. BACKGROUND

As increasing operating temperatures are expected in the next generation of nuclear reactors, materials with low creep rates and improved high temperature characteristics are essential. Components on the primary side of fission reactors will be exposed to radiation, temperatures up to 600°C, and corrosive environments while not deforming significantly or requiring expensive downtime for maintenance and cleaning. While improvements in water chemistry control have somewhat reduced concerns for corrosion, materials with lower creep rates and higher yield strength at elevated temperatures will do the most to prolong the life of reactors [1]. Materials currently in use and under development have been reviewed by Zinkle (Figure 1). In addition to fusion reactors, structural materials for future use in fission reactors will also require increased yield strengths and low creep rates at similar operating temperatures.

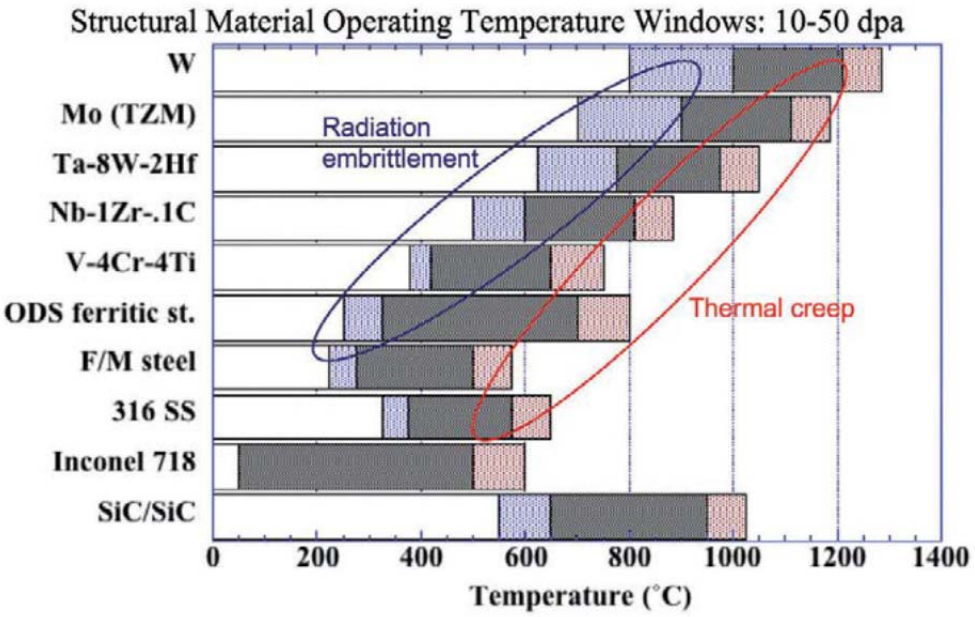

Figure 1. Temperature ranges for various structural materials subjected to intermediate doses. The operating temperature is usually limited by thermal creep on the high side and radiation embrittlement on the low side. From Zinkle [2]

Oxide dispersion strengthened (ODS) steels offer a possible solution to several issues faced in the development of next generation of reactors. ODS steels, MA956 in particular, are a type of steel strengthened by the addition of fine oxide particles, e.g. yttrium oxide (Y_2O_3). Added as a powder during mechanical alloying, these finely dispersed nanometer sized particles help strengthen the material by pinning dislocations. The materials may also possess ultra-fine grain size which strengthens the material through the Hall-Petch relationship. While ODS steels have high yield strengths at room temperatures (up to 900 MPa for fine grain MA956), they were designed for use in high temperature applications. In addition to increasing strength, finely dispersed oxide particles also act as sites to trap H and He, thus reducing the material's susceptibility to radiation induced swelling and embrittlement [3]. They also display resistance to creep at elevated temperatures. At 800°C, ODS steels demonstrate a secondary creep rate as low as 3×10^{-10} s^{-1} for an applied stress of 140 MPa [4]. ODS steels have also shown the ability to retain yield strengths at high temperatures. In recent work by Baker, MA956 retained one third of its yield strength (300 MPa) at 600°C [5]. Such high temperature performance indicated that ODS steels like MA956 could be used in several different applications in future fusion applications. A more comprehensive review of ODS steels for nuclear and high temperature applications can be found in work by Hoelzer, Kimura, and Klueh and Zinkle [1, 3, 6, 7].

Despite the promise of ODS steels for use in high temperature nuclear applications, joining this material through traditional means is highly problematic. The microstructural attributes which give this steel its strength can be severely altered by fusion welding techniques traditionally used for steels. Processes like gas tungsten arc welding and gas metal arc welding result in transport and agglomeration of the finely dispersed oxides to the surface of the weld pool, as well as significant alterations to the grain sizes upon solidification [8, 9]. The results are a significant reduction in yield strength across the weld and degraded properties in the large HAZ outside the weld pool. Other processes like laser beam welding and electro-spark deposition give similar results, coarsening the oxide particles which give ODS steels their strength [10, 11]. As melting

the base metal produces an undesirable microstructure, solid state joining techniques are necessary when joining ODS material.

Friction stir welding (FSW) is a possible solid state technique for joining ODS steels (Figure 2). FSW does not melt the base metal, and preserves many mechanical and microstructural properties that make ODS steels attractive. The process involves an extremely hard tool, usually polycrystalline cubic boron nitride (PCBN), which is forced to rotate between the working pieces. Friction between the tool shoulder and the plates heats the metal allowing plastic deformation and deposition of material behind the tool. A downward, or plunge force ensures consistent contact of the tool shoulder and the plate surface. This process produces very distinct regions across the welded plate. Along the weld centerline is the stir zone (SZ), which displays an "onion ring" texture from the deposition of plastically deformed material behind the tool [12]. On either side of the SZ is a thermo mechanically affected zone (TMAZ), which experiences significant plastic deformation and thermal gradients from friction as well as localized plasticity. Beyond the TMAZ is the heat affected zone (HAZ), which is exposed to heat from the weld but not plastic deformation. Beyond the HAZ is the base metal (BM), which remains unaffected by thermal gradients or plastic deformation. The side of the weld where tool rotation is in the same direction as the welding direction is the advancing side, with the other half denoted as the retreating side.

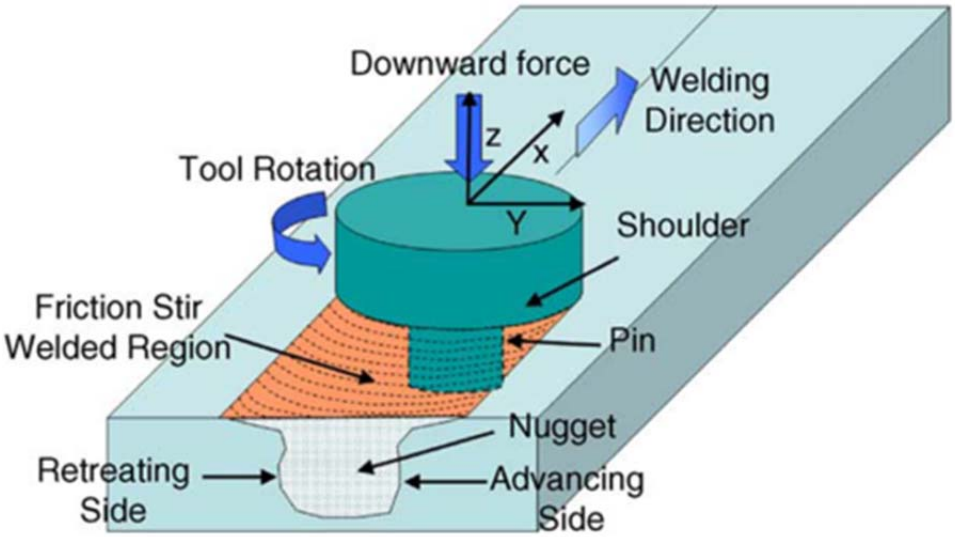

(a)

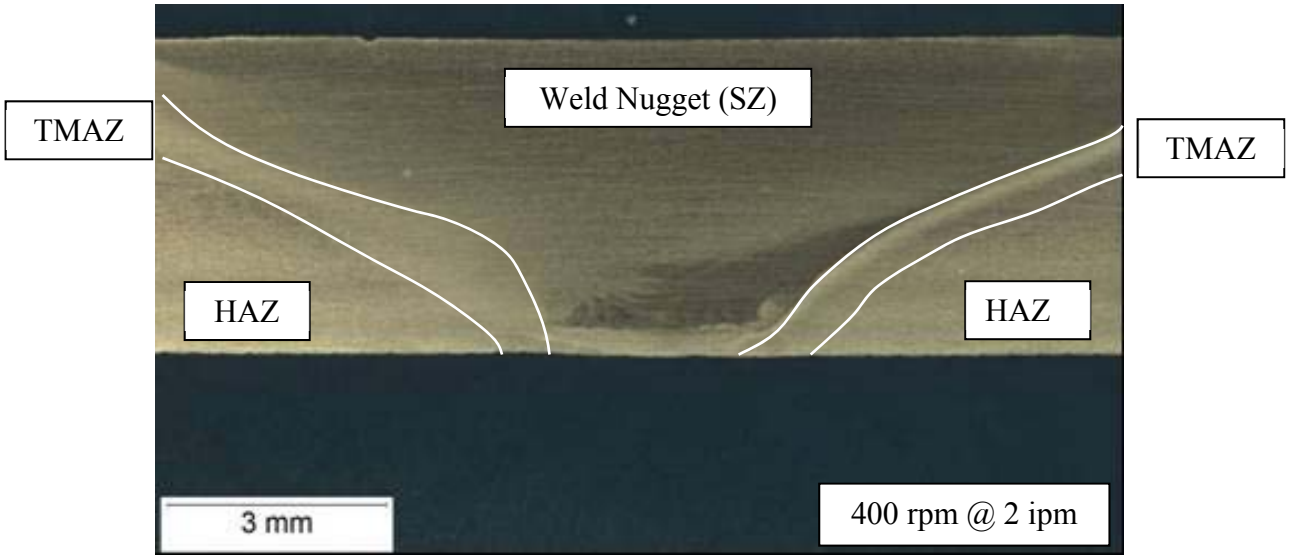

(b)

Figure 2. (a) A schematic of the FSW process. From Mishra [13]. The cross section from a FSW plate (b). From Baker [5].

Friction stir welds are characterized by the combination of tool rotational speed in revolutions per minute (rpm), the tool traverse speed in millimeters per minute (mmpm), and the plunge force of the tool against the plate. Combining rotational and traverse speed gives a 'weld pitch' or heat index (HI), in revolutions per millimeter, which is a rough indicator of the heat input to the weld. The simplified heat index of a set of welding conditions is given by [14]:

$$HI = \frac{\omega}{\nu} \tag{1}$$

where ω is the rotational speed in revolutions per minute (rpm) and ν is the welding traverse speed in millimeters per minute (mmpm). This relationship is not a direct measure of heat input to the weld, and will be used to compare the relative heat of different welding conditions. A higher weld pitch describes a higher heat index, a combination of high rotational speed and lower translational speed. Conversely, a lower rotational speed and higher traverse speed gives a lower weld pitch and lower heat index. Even at lower heat indices, FSW processes bring the material to 8090% of yield strength. Heat is generated by the FSW process through friction and plastic deformation between the tool and plate as well as plastic deformation in the TMAZ, which occurs just beyond the tool shoulder. Heat input is slightly asymmetric due to the relative velocity of the tool and the base plate and the tendency of plastic flow to occur on the retreating side of the tool [14].

Heat input from friction stir welding changes the mechanical properties of the base metal, but research demonstrates these effects can be mitigated by reducing the heat index of the weld. Analysis of grain and oxide sizes has been performed by Baker [5] and Han [12] for fine-grained ODS steels subjected to a variety of FSW conditions. Fine grained material has a grain size of less than 1 μm. Baker shows significant grain coarsening across the SZ, and a corresponding drop in hardness. While this lowers the room temperature yield strength and hardness, differences between FSW processed components and the BM are lessened at elevated temperatures (Figure 3). From tensile tests at room temperature, all FSW conditions reduced the yield strength of the BM. The highest heat input condition (500/25) resulted in a 42% reduction in yield strength, while lower heat input conditions reduced heat input by nearly the same amount. At 600°C, reductions in yield strength from FSW are lower for all conditions. The lowest heat input condition (400/100) resulted in a 19% reduction in yield strength while the highest heat input condition (500/25) resulted in a 33% reduction in yield strength [5]. At operating

temperature, only a 19% loss in yield strength from FSW demonstrates the potential for joining ODS steels like MA956.

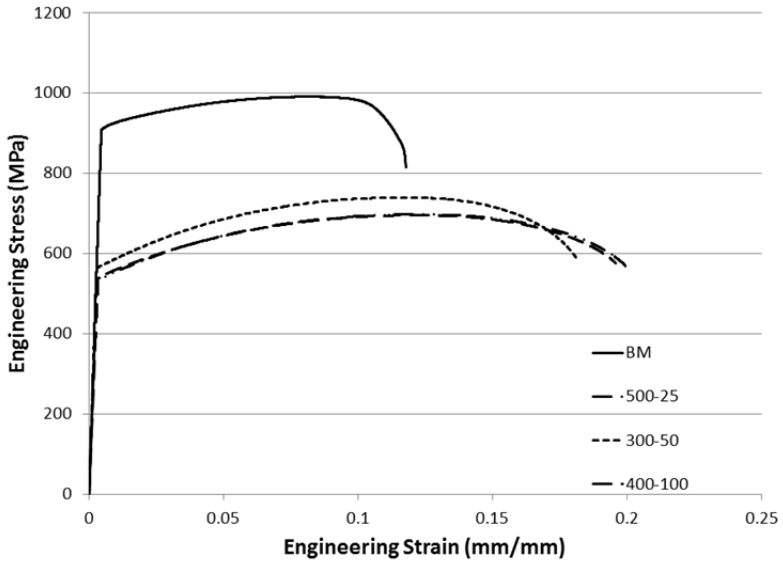

(a)

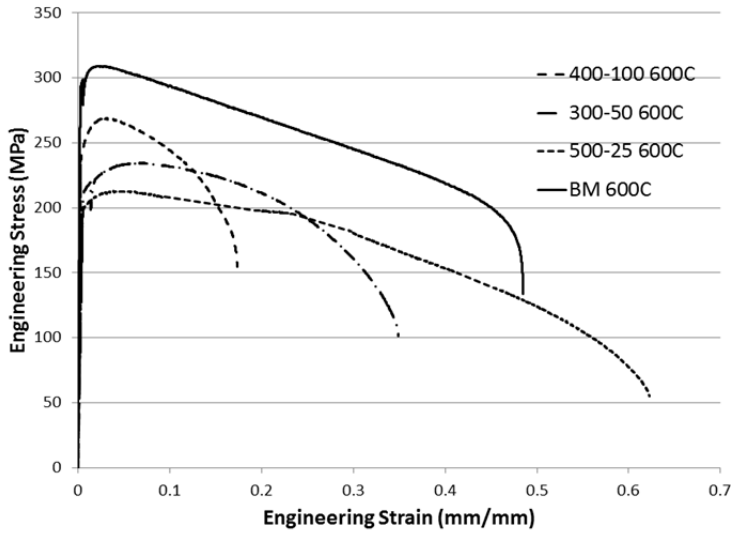

(b)

Figure 3. Engineering stress/strain curves for FSW MA956 at room temperature (a) and 600°C (b) From Baker [5]

While reductions in yield strength in FSW can be minimized by lowering the heat index, residual stresses pose a problem. As in all welds, the presence of thermal gradients in constrained pieces produces uneven contractions across the weld. This results in residual stresses as heated material is not allowed to contract. Figure 4 shows constrained, heated material that is not allowed to contract. The red region indicates the size of the heated section without restraint. Welding constraints and cooler material force the heated region to occupy the bold region upon cooling. This causes the development of residual stresses. Stresses along the weld centerline will be tensile, as the still heated material ties to contract but is restrained by the cooler metal around it and the physical restraints on the plates. For fusion weld, tensile stresses will peak at the center of the weld and decrease away from the weld centerline. Tensile stresses in the weld nugget will be balanced by compressive stresses further from the weld as the total force on the plate is zero. The shape of the profile and maximum values are determined by thermal gradients. Larger thermal gradients cause a greater mismatch in cooling rates and will lead to larger tensile residual stresses with a narrower tensile region. The FSW residual stress profile differs from a fusion weld profile due to the addition of extensive plastic deformation in the SZ. Peak tensile residual stresses will occur just beyond the tool shoulder and not along the centerline as coarse grains in the SZ cannot support the same stresses as the BM. The region just beyond the tool shoulder still retains the fine grains of the parent material as well as the large thermal gradients necessary to support large residual stresses. While not initially apparent, a larger heat input will likely result in a more shallow thermal gradient, and smaller residual stresses across the weld profile.

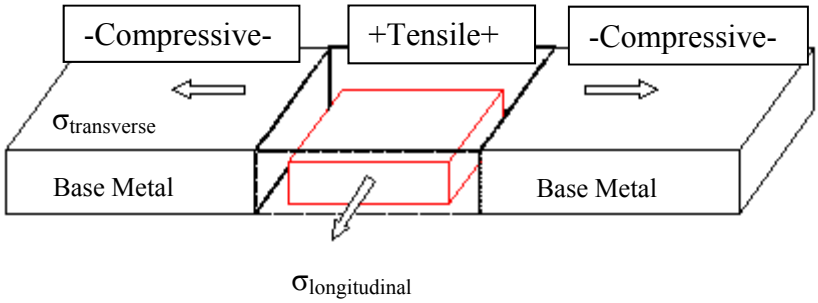

Figure 4. A simplified example of residual stresses developed during welding. The red region represents the size of the heated region upon cooling in the absence of constraint. The bold region represents the actual area the cooled metal will occupy in the presence of tensile residual stresses. The actual heated region has many more sub-regions with different cooling rates, and the mismatch in their contraction will result in residual stresses.

While the base material does not actually melt, the extreme thermal gradients produced by fusion welding are also present in FSW processes. Like fusion welding, the uneven cooling rates of heat affected materials generate residual stresses across the base metal and weld nugget. In a fusion weld, the base metal becomes molten while in FSW, only 80% of the melting temperature is reached. The heating is localized, and causes significant thermal gradients from the highest temperatures in the weld nugget to the relatively cold base metal. The generated thermal gradients and uneven cooling result in tensile residual stresses along and across the welding direction. FSW also involves stresses generated by plastic deformation from the tool rotating and translating through the base material, though this effect is complicated and not fully understood [14]. The thermo-mechanical process produces three dimensional residual stresses, as non-uniform cooling through the plate thickness will likely produce a stress normal to the plate. The largest and most important residual stresses are those along the welding direction, longitudinal stress, and those which run across the weld, transverse stresses.

The magnitudes of residual stresses generated by FSW have been measured for a variety of materials. In FSW of AA5083, Peel [15] showed that longitudinal residual stresses can reach up to 40% of the yield strength in the thermo-mechanically affected zone (TMAZ), where FSW reduced the 0.2% offset yield strength in the stir zone (SZ) from 392 to 147 MPa (Figure 5). FSW modeling by Chen [16] and Bastier [17] predict that the maximum longitudinal stresses are 4050% of yield in AA7050 and 6061-T6,

respectively. Work done by Steuwer et al. [18] on HSLA-65 steel demonstrated a peak longitudinal residual stress over 80% of the nominal yield strength. Reynolds [19] observed a similar phenomenon in SS 314 where the maximum longitudinal residual stress was 80% of yield for some conditions. In an alloy nearly identical to MA956, Mathon [20] performed a residual stress analysis for a single set of welding condition and found that residual stresses on the advancing side of the weld can be as high as 50% of the yield strength of the base metal. Stresses of this magnitude are significant as they drastically reduce the fatigue life of FSW components. While some studies examine the microstructural evolution for ODS steels after FSW, very little is known about the effect that changing heat input has on the residual stress distribution. Thus it is essential to characterize the residual stress as a function of heat index in ODS steels due to the unique nature of the microstructure.

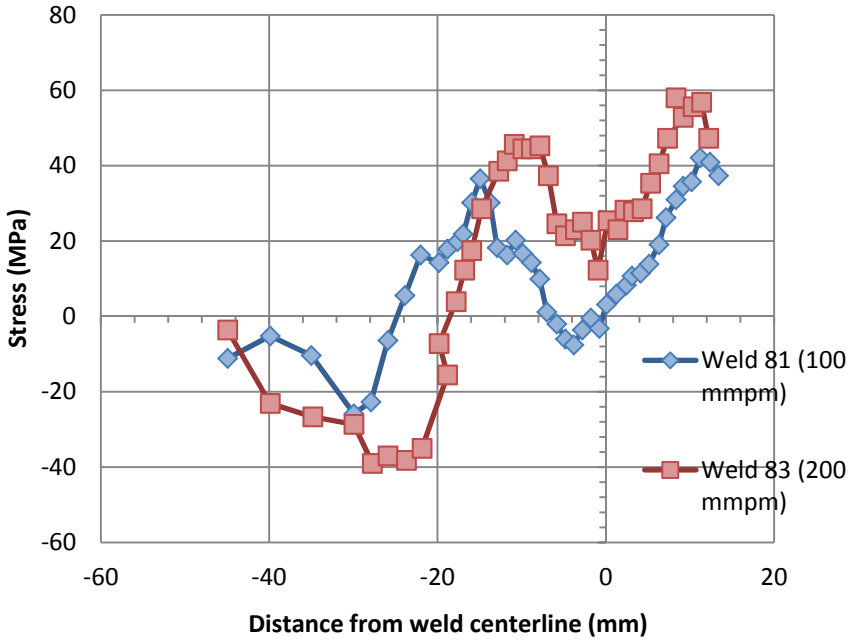

(a)

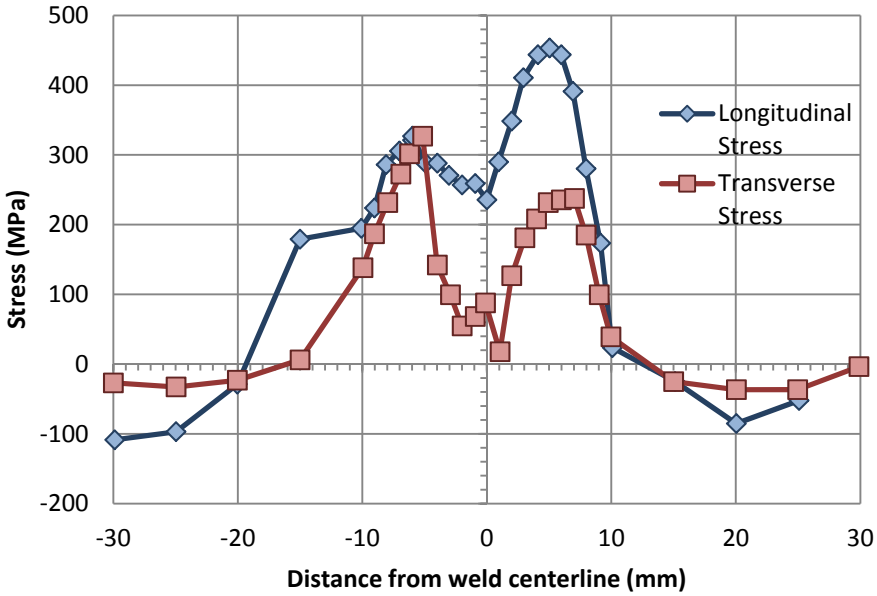

(b)

Figure 5. (a) Residual stress profiles for the FSW of AA 5083. From Peel [15]. (b) The residual stress profile across PM2000, an ODS steel nearly identical to MA956. From Mathon [20].

The spatial distribution of residual stresses produced by FSW share several key characteristics across the materials examined in the literature. Regardless of material, all longitudinal stress profiles displayed an 'M' shape, with tensile maxima occurring in the TMAZ just beyond the tool shoulder. Moving into the base metal, the tensile stresses rapidly dissipate and are balanced by smaller compressive stresses. In the stir zone, the stresses are reduced from the peak values but are generally still tensile. This reduction in stress level may be caused by the higher temperatures under the tool which weakens the material significantly along the weld line [18]. In addition, grain size has been observed to coarsen in the stir zone of many alloys. While most published results do not make a point of it, Mathon [20] demonstrates profiles of marked asymmetry in PM2000, an alloy nearly identical to MA956, where peak longitudinal stresses are much higher on the advancing side versus the retreating side.

B. X-RAY DIFFRACTION FOR MEASUREMENT OF RESIDUAL STRESS

This research will use x-ray diffraction techniques to examine the relationship between heat input and the longitudinal residual stress distribution to evaluate how changing weld parameters affect the stress profile.

X-ray diffraction measures the elastic strain at the surface of a stressed sample. The stress is calculated from the experimentally measured strain using linear elasticity theory. The atomic lattice of the material serves as a strain gage for the measurement (Figure 6). When x-rays interact with atoms in a crystalline material, rays are scattered in all directions. Increased intensity of this scattered beam occurs at angles where the path difference between two incoming waves is equal to an integer multiple of the incoming wavelength.

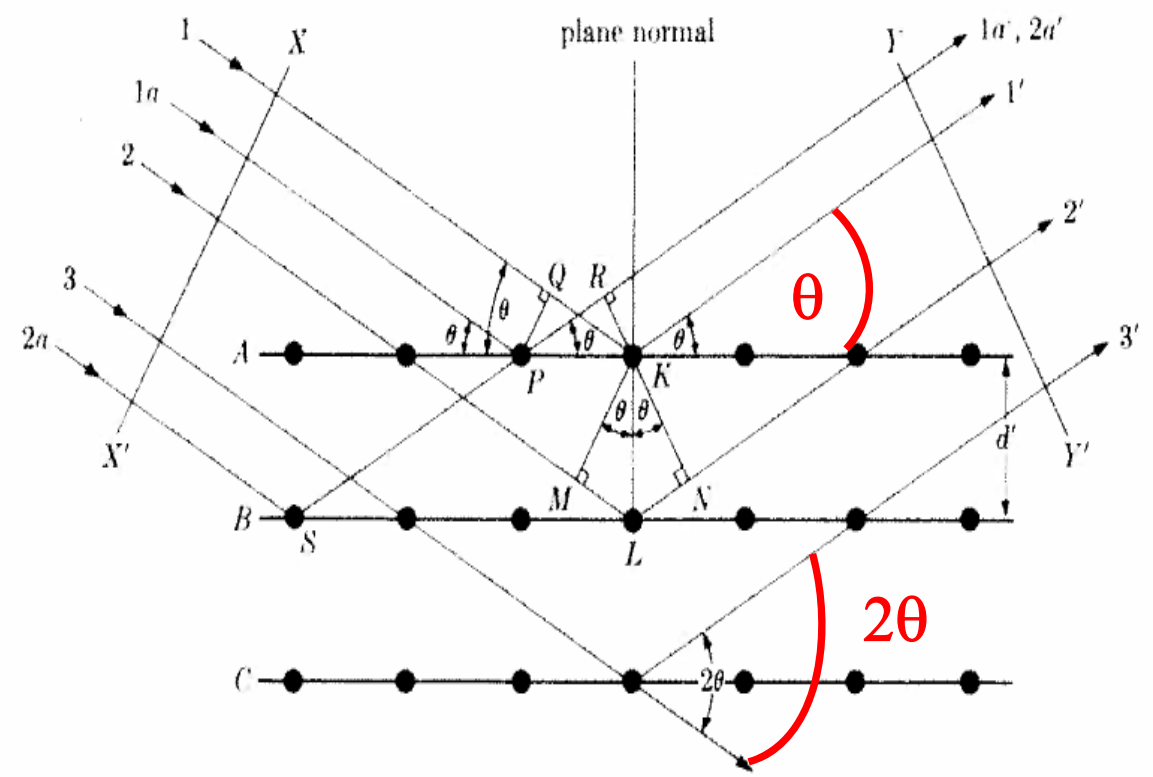

Figure 6. A diagram showing diffraction occurring according to Bragg's Law. From Cullity [21]

This critical angle is called the Bragg angle and diffraction occurs only when the conditions from Bragg's Law are met:

$$d = \frac{\lambda}{2sin(\theta)} \tag{2}$$

Where d is the plane spacing, λ is the wavelength of the radiation used, and θ is half of the measured diffraction angle (2θ). Residual strains in the material will change the planar spacing of atoms differently according to their angle from the surface normal (Figure 7). For example, the third set of planes will have a different spacing than set one or two in the presence of a residual stress. In the absence of stress, planes of the same family (e.g., {211}) will have the same planar spacing regardless of orientation.

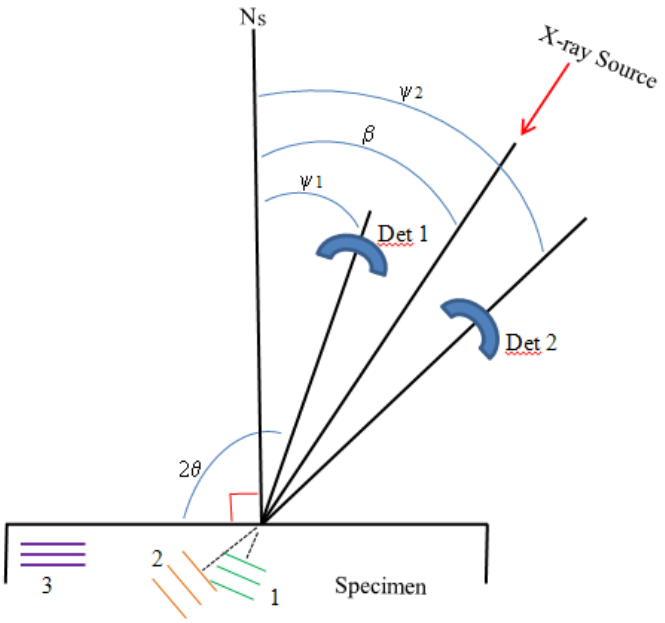

Figure 7. A diagram of different planar spacing due to residual stress. Ψ angles are normal to the measured plane. In this experiment {211} planes were used. From Banazwski [22].

When diffraction measurements are made on this unstressed polycrystalline material, the diffraction peaks should share the same Bragg angle (Figure 8). In the first image, a diffraction pattern taken on a stress free powder (<10 MPa) at different ψ angles shows almost no change in peak position. The second image demonstrates the peak shift which occurs in the presence of a significant (-502 MPa) residual stress. These differences in planar spacing can be used to measure the strains from which a residual stress tensor may be calculated.

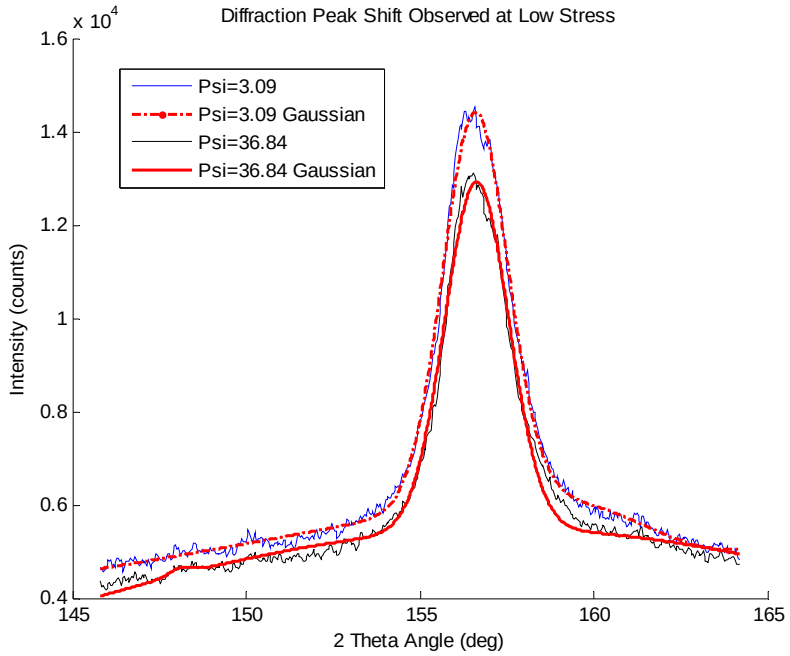

(a)

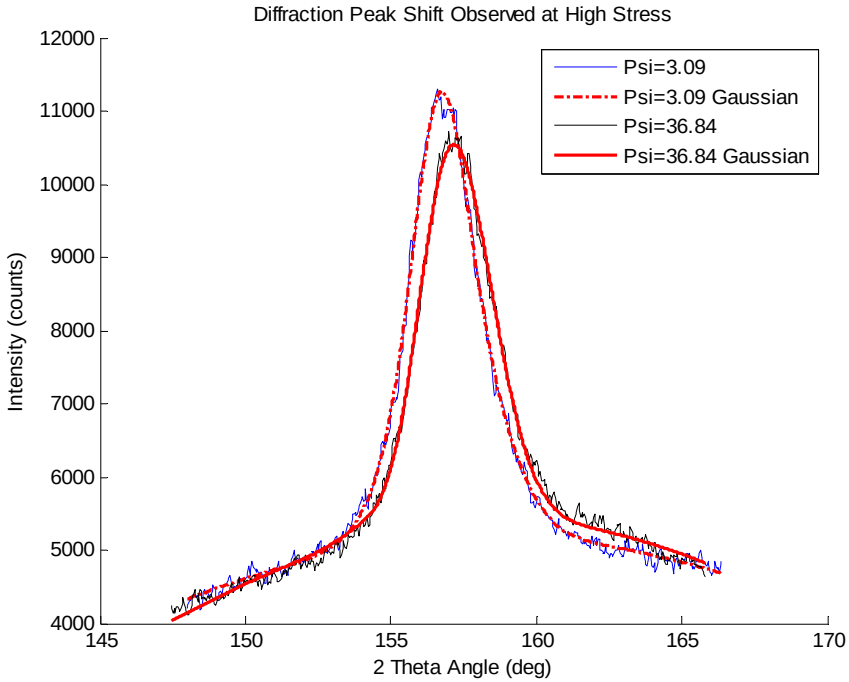

(b)

Figure 8. Peak shifts in low stress (a) and high stress (b) samples at ψ = 3.09° and 36.84°. While (b) was stressed to -502 MPa, the diffraction peak shift is small. This shows how even small lattice strains can produce large stresses.

Like other x-ray diffraction techniques, the multiple exposure technique (MET) collects the position of a single diffraction peak at a variety of ψ angles and Φ=0° to calculate stress using the "$\sin^2\psi$" technique (Figure 9). This measurement collects diffraction peaks at one Φ angle, so only one principal stress is measured. If the sample is oriented so that the head rotates around the y-axis, longitudinal stress is measured. Rotating the sample 90° so the head rotates around the x-axis allows measurement of the transverse stresses. This simplified method was used for calibration samples where the whole stress tensor was unnecessary.

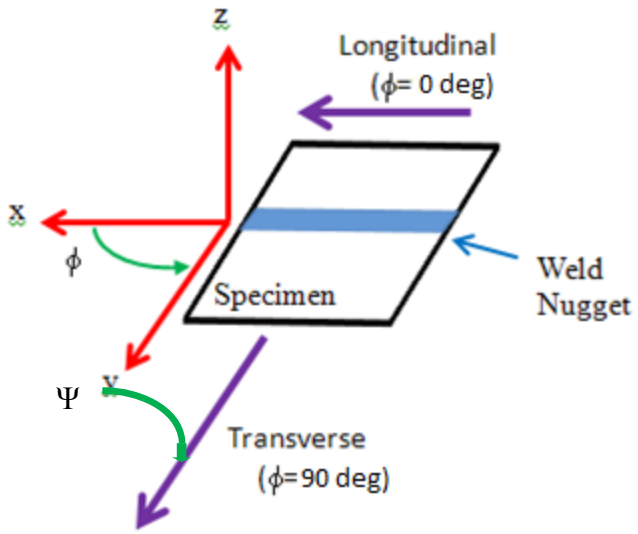

Figure 9. Sample geometry for this experiment. From Banazwski [22].

Once the planar spacing was known for several ψ angles, a "d vs. $\sin^2\psi$" plot was generated. As there is normally a linear relationship between d and $\sin^2\psi$, the slope of this line is proportional to the stress at the measured phi angle. This comes from the general case of Hooke's Law combined with the strain equation [23]:

$$\varepsilon_{\Phi\psi} = \frac{1+\nu}{E}\{\sigma_{11}cos^2(\Phi) + \sigma_{12}\,sin(2\Phi) + \sigma_{22}sin^2(\Phi) - \sigma_{33}\}sin^2\psi + \frac{1+\nu}{E}\sigma_{33} - \frac{\nu}{E}\{\sigma_{11} + \sigma_{22} + \sigma_{33}\} + \frac{1+\nu}{E}\{\sigma_{13}cos(\Phi) + \sigma_{23}\,sin(\Phi)\}sin2\psi \quad (3)$$

and

$$\varepsilon_{\Phi\psi} = \frac{d_{\Phi\psi} - d_0}{d_0} \quad (4)$$

where Φ is the angle from the y-axis in the plate surface and ψ is the angle between the normal of the plate surface and the planes of interest. Lattice spacing $d_{\Phi\psi}$ is the planar spacing measured at each angle and d_0 is the unstressed lattice spacing. As the measurement is conducted at φ = 0° and plane stress condition is assumed ($\sigma_{33} = \sigma_{13} = \sigma_{23} = 0$), the above equation simplifies to:

$$\varepsilon_{\psi} = \frac{1+\nu}{E}\sigma_{\Phi} sin^2\psi - \frac{\nu}{E}(\sigma_{11} + \sigma_{22}) \quad (5)$$

where σ_{Φ} is the stress of interest. The x-ray elastic constants were supplied by Proto Manufacturing for ferritic steel:

$$\frac{E}{\nu} = 783.1\ GPa\ and\ \frac{E}{1+\nu} = 168.9\ GPa \quad (6)$$

where E is the Young's Modulus, and ν is the Poisson's ratio for ferritic steel.

The stress of interest will simply be the slope in Figure 10. Note the difference in slope between the two curves. In the first plot, there is almost no difference in planar spacing across all measured psi angles (Figure 10A). The resulting curve has an extremely small slope. Comparatively, the second plot has a much larger slope resulting from changes in lattice spacing at different psi angles (Figure 10B). Both plots have negative slopes, which indicate compressive residual stresses. Splitting of the curves indicated the presence of a small, out of plane shear, τ_{i3}.

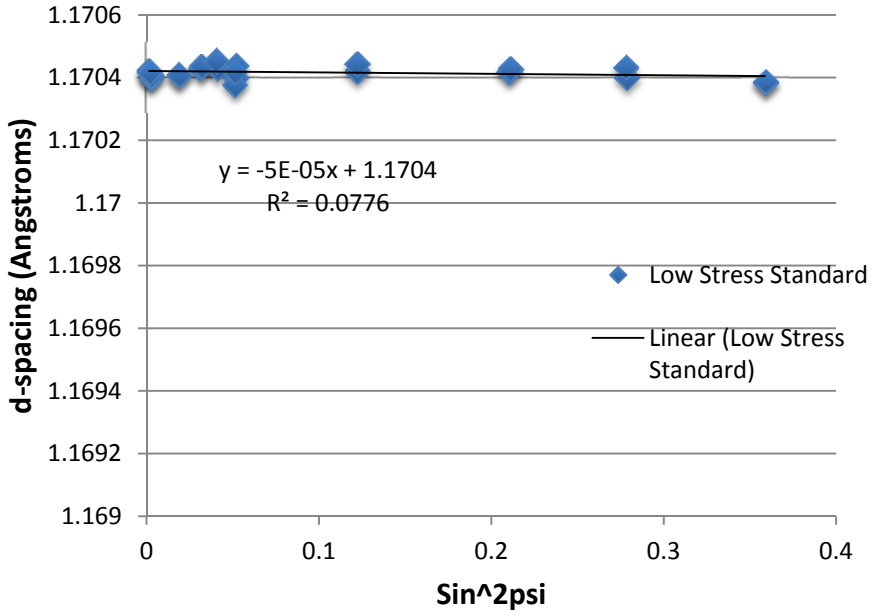

(a)

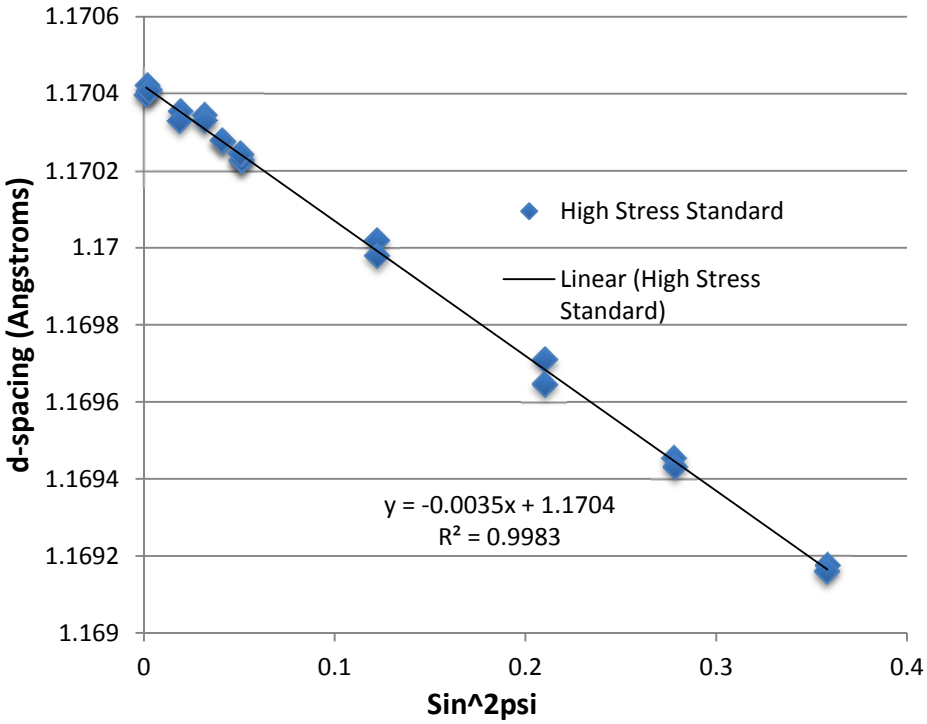

(b)

Figure 10. A d vs. $\sin^2\psi$ plot for a stress free ferritic steel powder (a) and a high stress ferritic steel standard (-502 MPa) (b).

While the MET scans determine the stress in one direction at the point of interest, the triaxial method determines the whole stress tensor. In this case, no plane stress assumptions are made, so more measurements are required to populate the strain tensor.

If measurements are only taken at Φ = 0°, important terms drop out of the equation. For a full representation of the stress state, measurements must be taken at Φ = 0, 45, and 90°, with multiple ψ angles taken at each φ angle. This allows measurement of the principal stresses in two perpendicular directions, from which a maximum resolved shear stress may be calculated.

Once the stresses are calculated, maximum and minimum principal stresses are calculated using tensor transformations of the general form [23]:

$$\sigma'_{ij} = a_{ik}a_{jl}\sigma_{kl}, \tag{7}$$

where a_{ik} and a_{jl} are direction cosines and σ'_{ij} is the resolved stress tensor.

The error associated with this method of determining the stress tensor is small, but a distinction must be made between accuracy and precision with this method. Error bars are included in all stress measurements and stress tensors, but most are not visible as the error values are small (0.5 to 10 MPa). This results from the number of measurements taken at each point along the profile. As the stress tensor only has five unknowns, assuming the principal out of plane stress is zero, five independent measurements taken at three phi angles are necessary to solve the system of equations. For this experiment, 11 different β tilts (each with two ψ angles) were measured at each of three phi angles. The resulting system is over-determined, so values given for error indicate the precision of the fit rather than a true measure of accuracy. Not included in error calculations are uncertainties in the elastic constants, and effects from sample positioning and roughness which may have a large effect on final calculations but are difficult to quantify.

Another important limitation of residual stress measurement by x-ray diffraction is the depth from which diffraction information was collected. X-rays do not penetrate material like thermal neutrons, thus an effort must be made to determine actual penetration for a given material. The penetration of x-rays in a material is described by the following equation [21]:

$$I_x = I_0 e^{-(\frac{\mu}{\rho})\rho x} \tag{8}$$

Where I_x is the intensity of the initial beam, I_0, after distance x. The mass absorption coefficient $\frac{\mu}{\rho}$ is specific to the material for a certain wavelength of radiation. For MA956 irradiated by Cr X-rays, λ = 2.291 Å, $\frac{\mu}{\rho} = 141.96\ \frac{cm^2}{g}$, and $\rho = 7.439\ \frac{g}{cm^3}$. The plot of the natural log of the incident intensity over the collected intensity as a function of depth is shown in Figure 11.

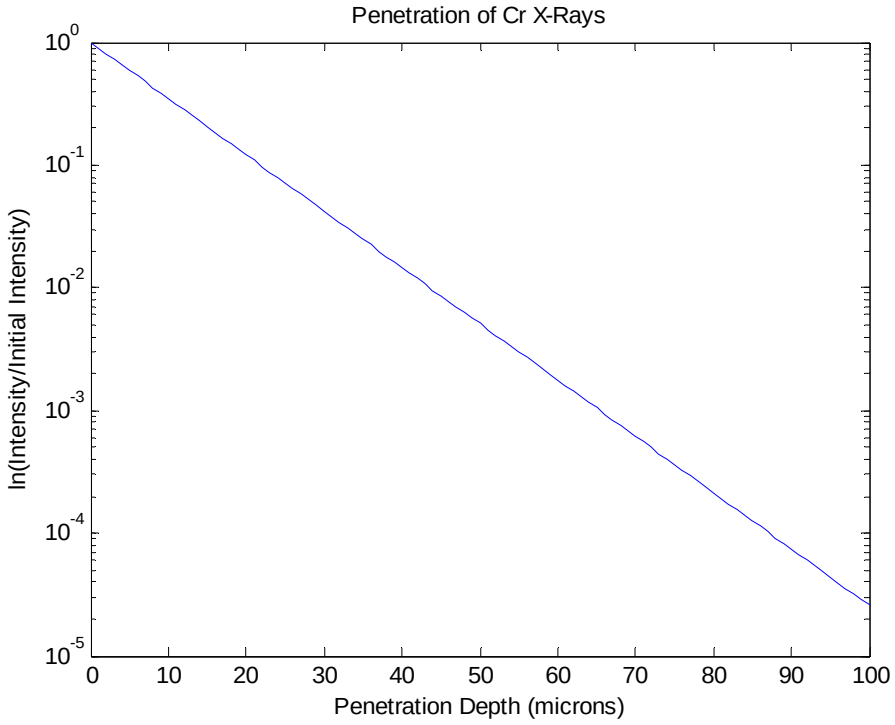

Figure 11. Calculated penetration of Cr x-rays into MA956.

After less than 90 μm, the intensity of the incident beam has been reduced to one ten-thousandth of its original strength. The diffracted beam still has to travel the same distance leaving the sample, so it is unlikely that any data is collected beyond a depth of~40 microns. With so little penetration available, electropolishing or the hole-drilling method is necessary to measure stress with depth. However, both of these methods are destructive and hole-drilling is intended to only perform plane stress measurements

around the hole [14]. Many non-destructive measurements of residual stress have been performed with neutron diffraction, which uses thermal neutrons instead of x-rays to determine changes in planar spacing. The neutron diffraction approach offers an advantage over x-ray diffraction as thermal neutrons penetrate much deeper and can be used to measure a volume averaged stress across a larger volume of the plate. As neutron diffraction techniques were not available during this thesis, we combined electropolishing with x-ray diffraction to measure residual stresses at different depths on the plate.

C. THESIS OBJECTIVES

- **Install and test a new x-ray residual stress instrument at NPS**. We will install and test the new Proto Manufacturing iXRD instrument, a dedicated x-ray diffractometer for measuring residual stress. Calibration will be performed using aluminum and steel samples and laboratory standards.
- **Measure the residual stress distributions around friction stir welds in ODS steel MA956 using x-ray diffraction.** We will use x-ray diffraction to measure the residual stress distributions across friction stir welds produced with weld pitch values chosen to increase the heat input during welding. We will perform triaxial measurements on two plates. In addition, we will determine if these stresses are affected by depth.
- **Determine the relationship between heat index (HI) to welds and the magnitude of resulting residual stresses.** We will use knowledge from the literature to explain the connection between the increase in heat index and the observed changes in residual stress. We will also connect these changes in residual stress to the known changes in microstructure and mechanical properties for this material.

II. EXPERIMENTAL METHODS

A. MA956 SPECIFICATIONS AND WELDING PARAMETERS

The material used in these experiments was MA956, a high Cr, ferritic, oxide dispersion strengthened (ODS) steel produced by Special Metals Inc. Its chemical composition is listed in Table 1.

C	Cr	Al	Ti	Y_2O_3	Mo	Mn	Ni	S	Si	P	Fe
0.023	19.93	4.75	0.39	0.51	0.02	0.09	0.04	0.008	0.08	0.006	Bal.

Table 1. Chemical composition of MA956. From Baker [5]

The alloy was canned and extruded at 1,100°C (2025°F) and hot rolled three times at 1,100°C over a period of 4 hours with reheating to 1,100°C for 30 minutes before and after each rolling. The final plate was machined to a thickness of 4 mm (0.157 inches) [5].

Friction stir welding was performed by MegaStir Technologies using a 25 mm diameter MS 80 grade polycrystalline cubic boron nitride (PCBN) tool with a convex scroll shoulder step spiral (CS4). The plunge force was a constant 17.8 kN [5]. Three different conditions were selected to test the residual stress distribution across a range of heat inputs. From highest to lowest heat input: 500 rpm/25 millimeters per minute (mmpm), 400 rpm/50 mmpm, 400 rpm/100 mmpm. These were all performed in one pass, changing conditions mid pass. The two plates provided by Lawrence Livermore National Laboratories were welded under identical conditions.

B. X-RAY DIFFRACTION

The residual stress measurements were performed with the iXRD Residual Stress Analyzer configured in bench-top mode from Proto Manufacturing (Figure 12). The instrumental setup included two position sensitive scintillation detectors (PSSD) collecting diffracted beams on either side of a collimator. Both detectors have 512 independent channels to measure diffracted intensity in counts and can be shifted to

center the diffraction peak on the display. Motors allow the head to translate 100 mm in the x, y, and z directions as well as rotate ~30° in the ψ direction and ~75° in the φ direction due to the sensitivity of the fiber optics used to carry the signal. While this instrument can perform strain measurements with several techniques, this experiment utilized the triaxial method to calculate the strain tensor.

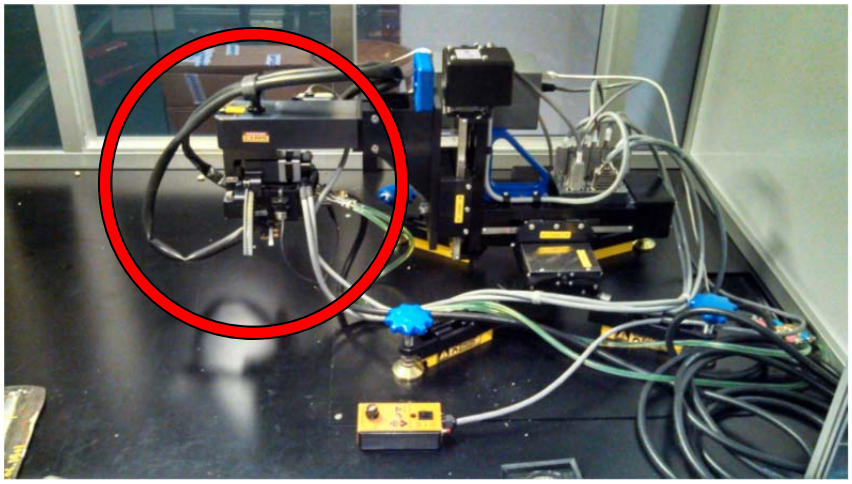

(a)

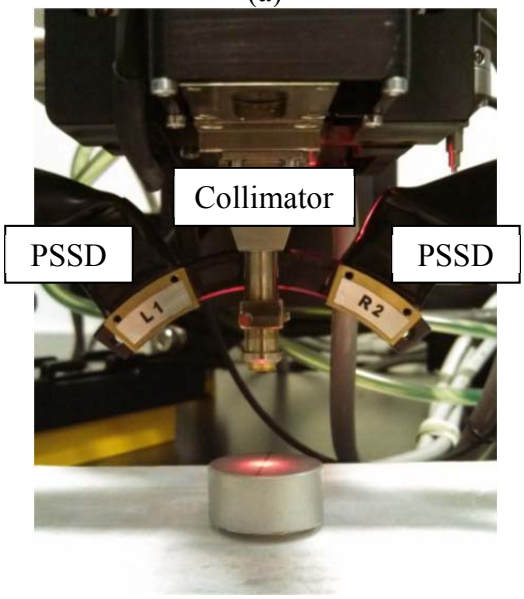

(b)

Figure 12. Proto Manufacturing's iXRD. Samples are measured under the head on the left side of the instrument (a). A close-up of the goniometer and the position sensitive scintillation detectors is given in (b). Chromium x-rays traveling through the collimator irradiate the sample. Left and right detectors are arranged to collect the diffracted beams.

To ensure accurate measurement of experimental strains, instrument accuracy was tested with several alignment procedures. Accurate rotation in the ψ and Φ directions was confirmed and a series of stress measurements were taken first with unstressed powders and later with high stress standards. Unstressed powder samples and high stress standards used the multiple exposure technique. All residual stress measurements were performed with Cr x-rays (λ=2.291 A), produced at an x-ray tube voltage of 20 kV and 4.0 mA, under the conditions listed in Table 2:

No. exposures	5
Time/Exposure	3 s
ψ Angles (deg)	±36.84, ±31.86, ±27.34, ±20.60, ±13.23, ±13.15, ±11.84, ±10.46, ±8.17 ±3.66, ±3.09
ψ oscillation	4°
Φ Angles	0°, 45°, 75°
Aperture Size	1 mm dia.
Peak {hkl}	-211
2θ	156.31°

Table 2. Triaxial stress measurements conditions used for measurements in Plate 1 and Plate 2 (MET scans on unstressed powder and high stress standard were taken with Φ=0° only)

Steel powder was collected on a slide to give a zero stress reference. The powder cannot support a stress and provides a random assortment of grains of varying orientations to eliminate anisotropy effects. The machine was also tested on a high stress standard. A calibration steel sample carefully stresses to a predetermined value of -502 ± 35 MPa from Proto Manufacturing was used. Normal and shear stress values of ±10 MPa for the stress free powders are acceptable, as are values within the error on the high stress standard. It should be noted that these shear stresses are the out-of-plane, τ_{i3}, components. All measured values fell within the specified range. Only the values from the first test are given in Table 3, but alignment was checked before mapping the residual stress distribution across each plate as well as before taking stress with depth measurements.

Stress-Free Powder MET Scans		
Scan	Stress, σ (MPa)	Shear, τ (MPa)
1	-6.12 ± 3.3	-1.0 ± 1.5
2	-0.90 ± 2.3	-2.1 ± 1.0
3	-7.08 ± 3.1	-3.5 ± 1.4
4	2.29 ± 2.3	-2.3 ± 1.0

High Stress MET Scans		
Scan	Stress, σ (MPa)	Shear, τ (MPa)
1	-507 ± 3.6	2.8 ± 1.6
2	-514 ± 3.9	1.1 ± 1.8
3	-508 ± 3.5	0.2 ± 1.6
4	-507 ± 2.9	2.1 ± 1.3

Table 3. Sample MET scans performed for instrument alignment

Triaxial stress measurements were taken at 5mm increments across the weld from the base metal (BM), across the heat affected zone (HAZ), and across the thermo-mechanically affected zone (TMAZ). To provide better resolution, 1 mm spatial increments were used across the stir zone (SZ). These were chosen to match the spacing in Mathon's paper on the residual stress distribution in PM2000, a nearly identical alloy. Residual stresses across FSW runs on two MA956 plates were determined. Figure 13 shows the positions of residual stress measurements taken across Plate 1. Residual stress profiles were taken approximately at the midpoint of each welding condition to ensure correct welding speed and rotational rate were reached, indicated by the red/green lines A, B, and C. Line A correspond to the 500 rpm/25 mmpm condition, line B corresponds to the 400 rpm/50 mmpm condition and line C corresponds to the 400 rpm/100 mmpm condition. Red lines indicate regions where triaxial measurements were performed with 5mm spacing while green regions were performed at 1 mm spacing to improve spatial resolution.

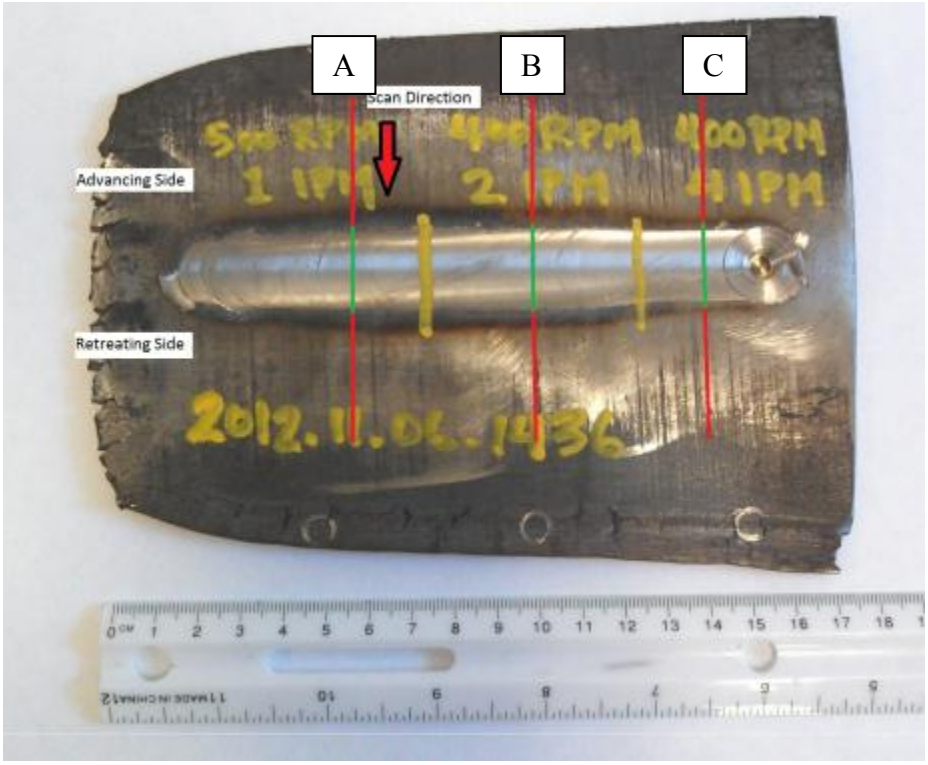

(a)

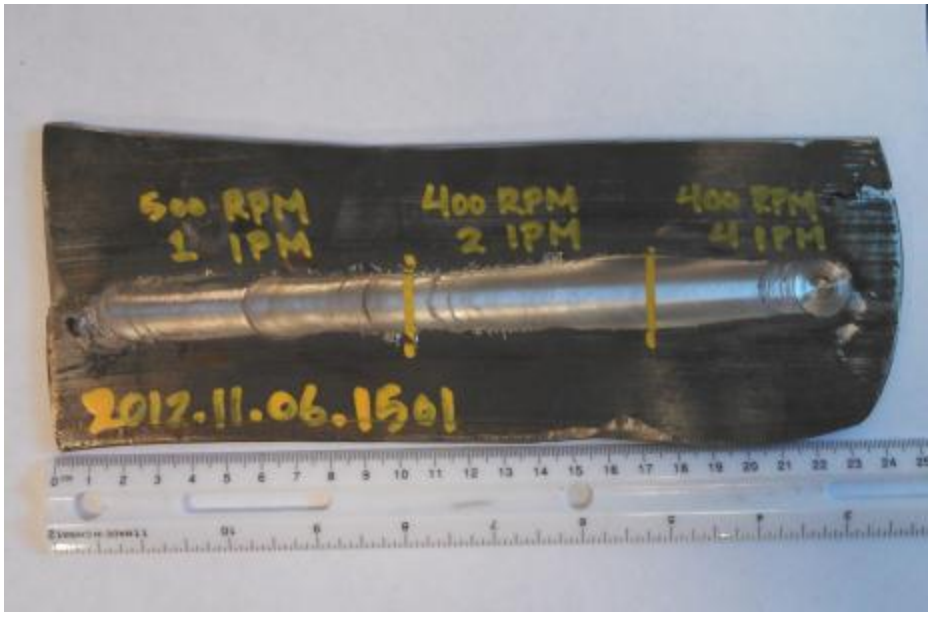

(b)

Figure 13. The two plates used in this analysis. The wider plate (a), will be referred to as Plate 1, while the narrow plate in (b) will be referred to as Plate 2. Scan locations and direction are shown as well as the locations of the advancing and retreating sides of the weld, which are consistent from Plate 1 to Plate 2.

Measurements for both plates used the same 5 mm spacing in the base metal and 1 mm spacing in the weld nugget, however the width of the stress profiles across the thin plates were smaller as less material was available. Scans on the wide plate included 45 mm on either side of the weld centerline while scans on the thin plate included 35 mm on each side of the centerline.

After profiles were taken across the welds of both plates, additional resolution was required to accurately determine the magnitude of the peak stress on the advancing side so a 10 mm profile with 1 mm spacing was centered on the advancing edge of the weld nugget.

Residual stress measurements were also taken as a function of depth. Electropolishing was utilized to remove material at four depths up to ~1 mm in two locations: 2 mm from the edge of the weld nugget and along the middle of the weld nugget. Both of these measurements were made at the 400 rpm/ 100 mmpm section of weld of the thin plate (Table 4).

	Position	
	2 mm from nugget	Centerline
Depth 1 (mm)	0.27	0.31
Depth 2 (mm)	0.52	0.51
Depth 3 (mm)	0.69	0.7
Depth 4 (mm)	0.94	1.08

Table 4. Depth measurements after electropolishing

Electropolishing was performed with Proto Manufacturing's "Electrolyte A" at an applied voltage of 50V and a resultant current of 2.2–3.0 A for approximately 160 s to reach each depth (Figure 14).

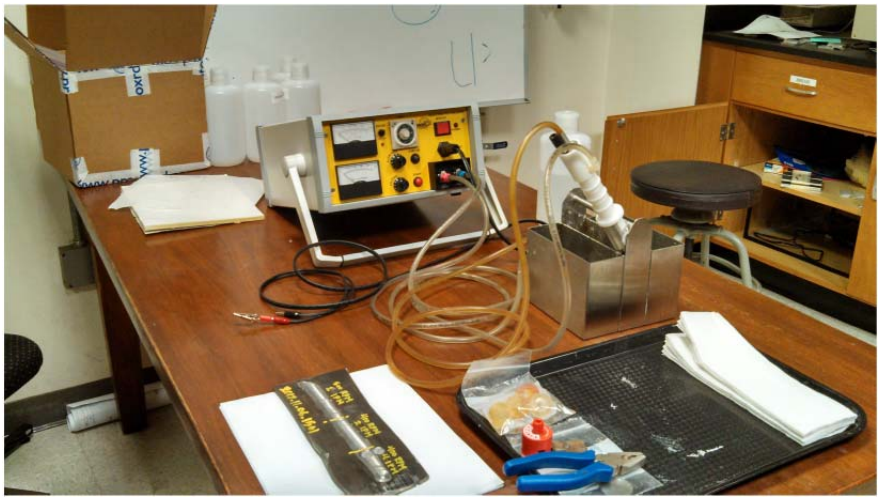

(a)

(b)

Figure 14. Proto Manufacturing's Electropolisher (a) and the position for stress at depth measurements (b)

The actual depth was measured using the auto-focusing pointer on the iXRD, which is accurate to 0.01 mm. Triaxial measurements were taken at each depth using the same conditions as the triaxial measurements for the cross weld scans: Cr X-rays (λ=2.291 A), produced at a tube voltage of 20 kV and 4.0 mA, {211} diffraction peak with an unstressed Bragg angle of 156.31°, 1 mm aperture collecting 5 scans per angle at 3 seconds per scan.

THIS PAGE INTENTIONALLY LEFT BLANK

III. EXPERIMENTAL RESULTS

A. RESIDUAL STRESS PROFILES

Each of the measured residual stress profiles across Plate 1 showed the "M" profile with varying degrees of intensity (Figure 15). Peak longitudinal stresses occur just beyond the weld nugget and tool shoulder, and are balanced by compressive stresses in the heat affected zones (HAZ) and base metal (BM). Due to the constraints on plate width, it is questionable whether or not the stress profile extends into the BM as only 45 mm is available on either side of the weld centerline. The profile is less pronounced at the highest heat input (HI) condition, 500/25, but as HI decreases, the "M" shape becomes more apparent. Peaks on the advancing and retreating sides are nearly equal in magnitude. Differences in peak tensile values between advancing and retreating sides in this profile range from 35–100 MPa.

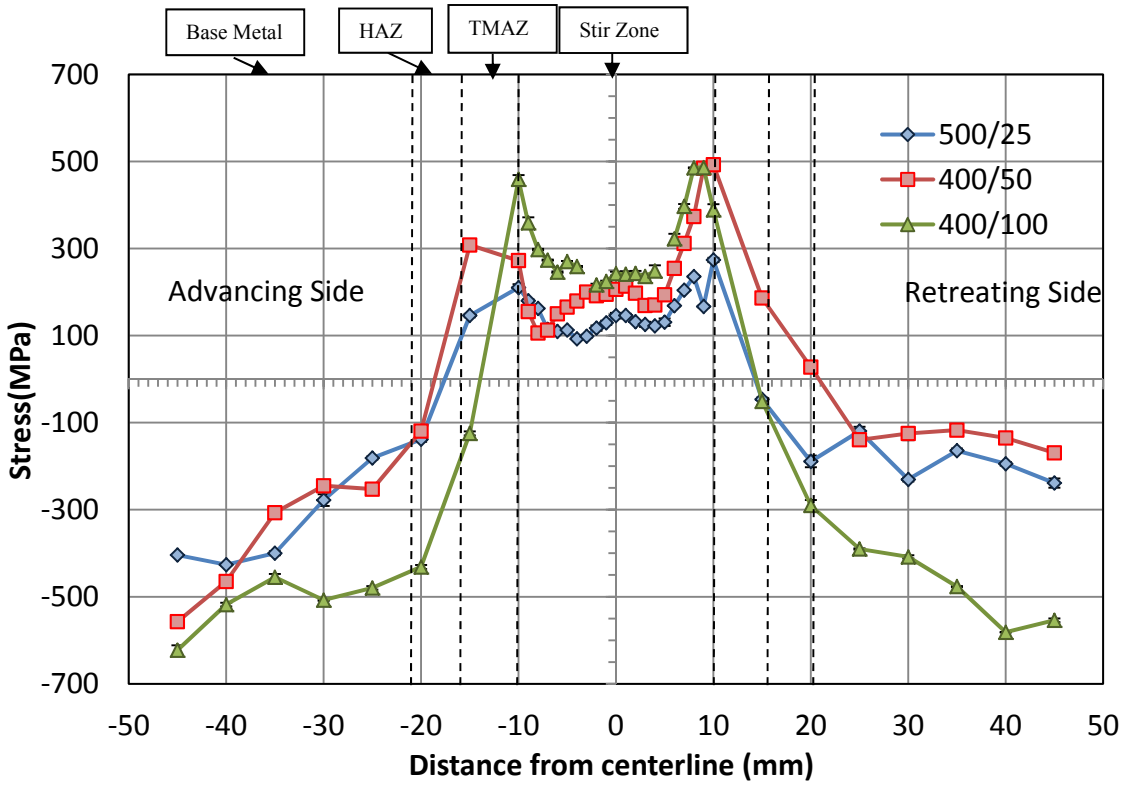

Figure 15. Longitudinal stress from the crown of Plate 1.

A more detailed view of the gradient in longitudinal stress confirms that that largest stresses are generated by the lowest heat input (Figure 16). Even with better spatial resolution on the advancing side, asymmetry between the peak stresses was not observed in this experiment.

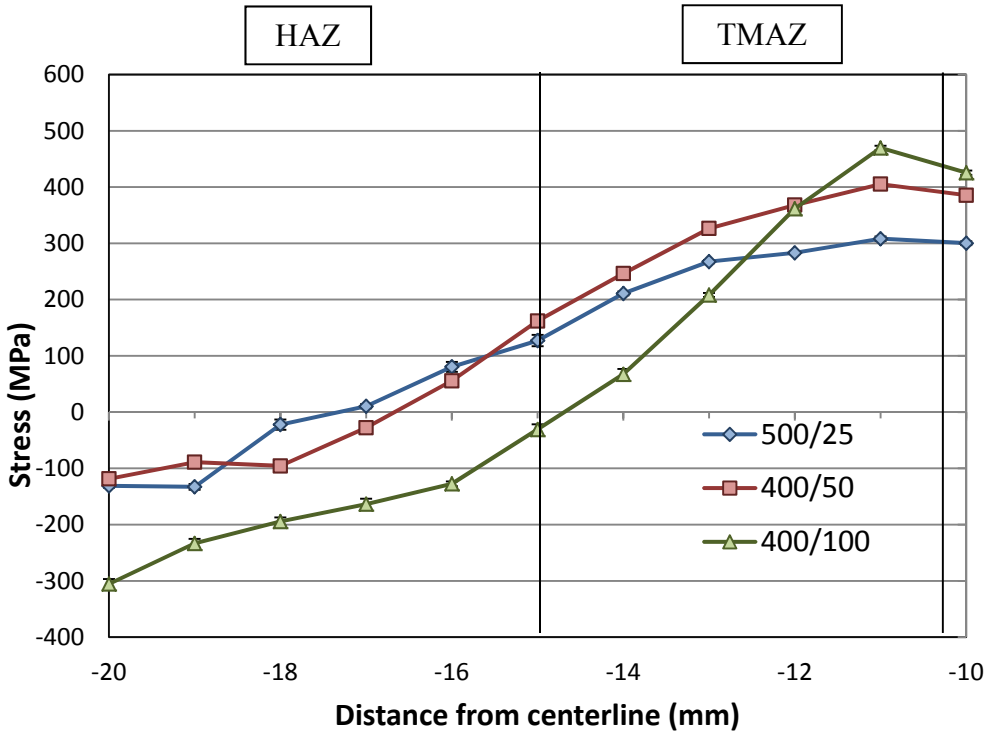

Figure 16. Longitudinal residual stress maximum values in the crown of Plate 1, on the advancing side (negative values for position always indicate advancing side of the weld nugget).

Stress measurements were repeated on Plate 2 with similar results (Figure 17). An "M" shaped profile was observed with no substantial asymmetry in the peak values. These peak values were also located just beyond the tool shoulder. The peak longitudinal stresses in Plate 2 increased with a decreasing HI from ~200 MPa for the 500/25 condition to almost 900 MPa for the 400/100 condition. The local stress minimum in the weld nugget also increased as HI decreased. It is interesting to note that the peaks on Plate 2 are higher, and the local minimums in the stir zone are lower than in Plate 1. Due to the scarcity of MA956, the second plate was narrower and therefore less likely to contain material unaffected by heat from the weld.

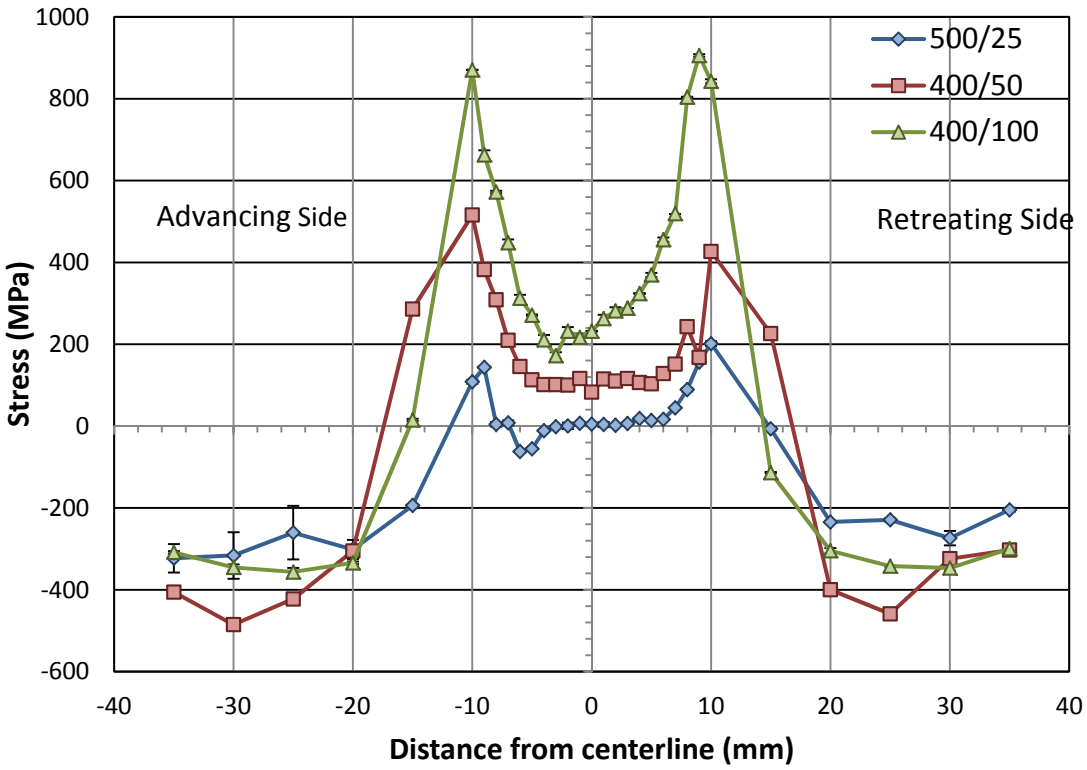

Figure 17. Longitudinal stress profile from the crown of Plate 2.

While longitudinal stresses are the most significant in the discussion of fatigue life in welded parts as they are the largest, transverse and other stress components are also important. The full stress tensor was calculated for each point along each stress profile, so the transverse and shear stresses, as well as any out of plane components, are available (Figure 18). Like the longitudinal stresses, transverse stresses also increased with lower HI. In the tensile region, values ranged from -10 MPa (nearly zero) for the 500/25 condition to 233 MPa for the 400/100 condition. As expected, transverse stresses were lower than longitudinal stresses at the same point on each plate, but followed the same trends as longitudinal stresses. Interestingly, the transverse stresses evolve in more of a "W" pattern than the "M" patter observed for the longitudinal stresses. It is also important to ensure that the out of plane components (σ_{13} and σ_{23}) are zero or nearly zero at the surface (Figure 19, 20). The third principal stress by definition must be zero at the surface, but these values may increase with depth and will become more important in the discussion of stress with depth.

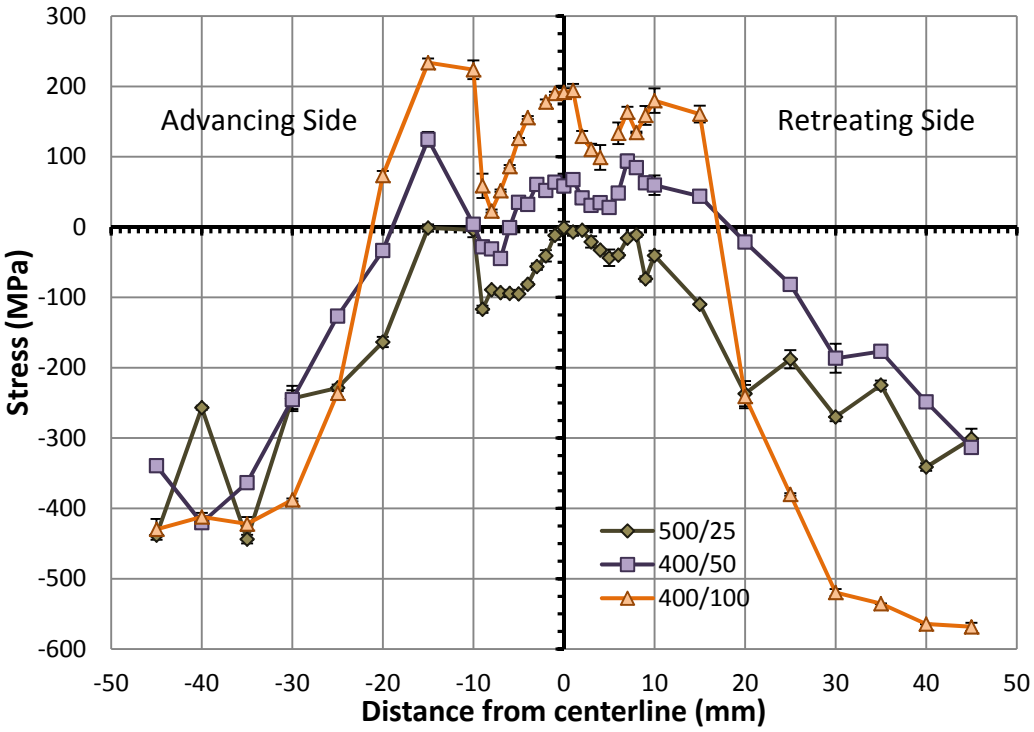

Figure 18. Transverse stress from the crown of Plate 1

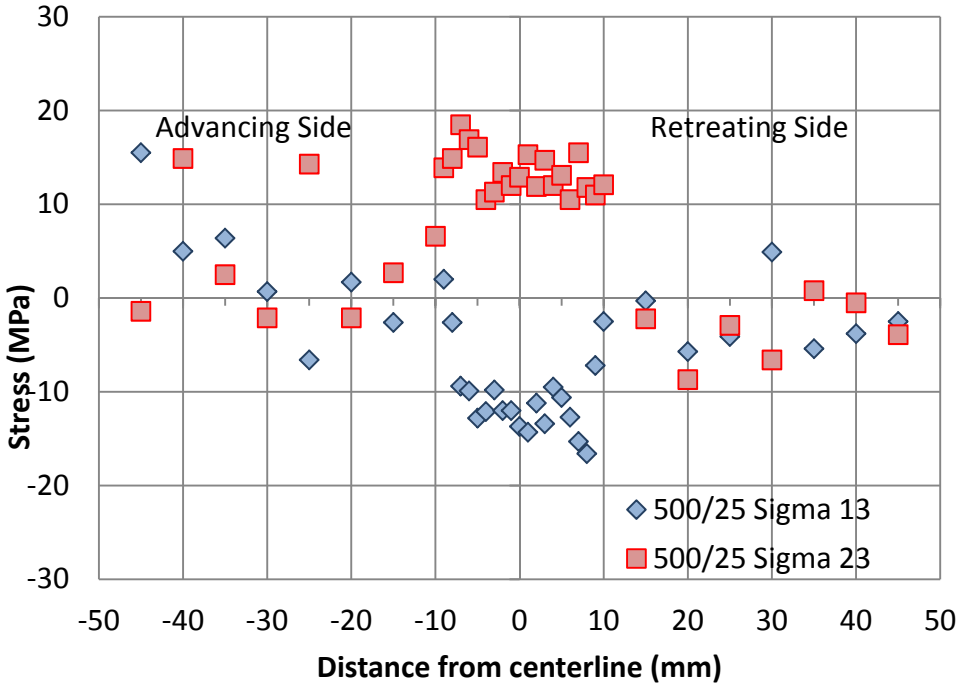

Figure 19. Out of plane stress for the 500/25 condition in Plate 1

$$\begin{pmatrix} -400.1 & -97.51 & 6.43 \\ - & -443.0 & 2.5 \\ - & - & 0.0 \end{pmatrix} \pm \begin{pmatrix} 4.6 & 7.0 & 1.0 \\ - & 6.2 & 1.1 \\ - & - & 2.7 \end{pmatrix}$$

(a)

$$\begin{pmatrix} 146.0 & -45.5 & -13.7 \\ - & -1.0 & 12.9 \\ - & - & 0.0 \end{pmatrix} \pm \begin{pmatrix} 6.4 & 9.7 & 1.5 \\ - & 8.6 & 1.5 \\ - & - & 3.6 \end{pmatrix}$$

(b)

$$\begin{pmatrix} 206.1 & -74.1 & -10.2 \\ - & 58.3 & 17.4 \\ - & - & 0.0 \end{pmatrix} \pm \begin{pmatrix} 4.2 & 6.5 & 1.0 \\ - & 5.7 & 1.0 \\ - & - & 2.5 \end{pmatrix}$$

(c)

$$\begin{pmatrix} 242.4 & -104.7 & 3.7 \\ - & 191.7 & 17.8 \\ - & - & 0.0 \end{pmatrix} \pm \begin{pmatrix} 4.3 & 6.6 & 1.0 \\ - & 5.9 & 1.1 \\ - & - & 2.6 \end{pmatrix}$$

(d)

Figure 20. Residual stress tensors for 500/25 BM (a), 500/25 SZ (B), 400/50 SZ (c) and 400/100 SZ (d). All stresses reported in MPa. Tensors are symmetric.

B. RESIDUAL STRESSES AS A FUNCTION OF DEPTH FROM THE SURFACE

The residual stresses measured as a function of depth from the surface showed different trends for the different positions across the weld (Figure 21). In the weld centerline (stir zone), the longitudinal stresses do not change significantly down to a depth of 1 mm below the surface. In contrast, the longitudinal stresses in the TMAZ decreased significantly with depth. From 900 MPa at the surface, the longitudinal stress peak decreased to less than 600 MPa. Example stress tensors from depths at each condition are given (Figure 22).

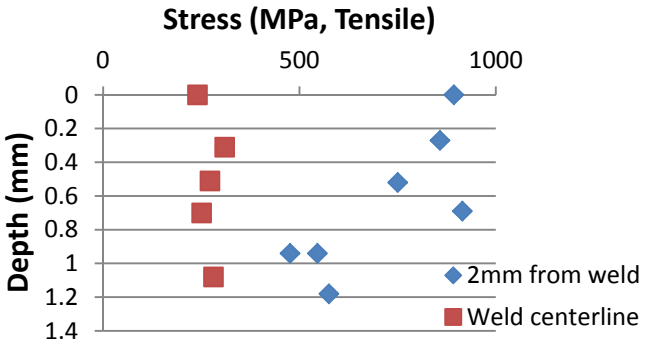

Figure 21. Longitudinal stress with depth measurements for the 400/100 condition

$$\begin{pmatrix} 240.3 & -17.03 & 18.53 \\ - & -198.3 & 19.01 \\ - & - & 0.0 \end{pmatrix} \pm \begin{pmatrix} 1.76 & 2.68 & 0.41 \\ - & 2.37 & 0.43 \\ - & - & 1.04 \end{pmatrix} Surface$$

$$\begin{pmatrix} 272.19 & 15.91 & 22.40 \\ - & -47.66 & 4.99 \\ - & - & 0.0 \end{pmatrix} \pm \begin{pmatrix} 0.73 & 1.11 & 0.17 \\ - & 0.98 & 0.18 \\ - & - & 0.43 \end{pmatrix} (Depth = 0.51\, mm)$$

$$\begin{pmatrix} 280.9 & 6.72 & 11.21 \\ - & 4.79 & 7.48 \\ - & - & 0.0 \end{pmatrix} \pm \begin{pmatrix} 1.19 & 1.81 & 0.28 \\ - & 1.60 & 0.29 \\ - & - & 0.70 \end{pmatrix} (Depth = 1.08\, mm)$$

(a)

$$\begin{pmatrix} 893.55 & -134.87 & 43.50 \\ - & 82.12 & 16.46 \\ - & - & 0.0 \end{pmatrix} \pm \begin{pmatrix} 2.34 & 3.57 & 0.54 \\ - & 3.15 & 0.57 \\ - & - & 1.39 \end{pmatrix} (Surface)$$

$$\begin{pmatrix} 749 & -129.0 & 34.13 \\ - & 318.85 & 7.45 \\ - & - & 0.0 \end{pmatrix} \pm \begin{pmatrix} 10.76 & 16.38 & 2.49 \\ - & 14.45 & 2.60 \\ - & - & 6.36 \end{pmatrix} (D = 0.52\, mm)$$

$$\begin{pmatrix} 476.0 & 89.85 & -0.51 \\ - & 306.9 & 20.15 \\ - & - & 0.0 \end{pmatrix} \pm \begin{pmatrix} 1.69 & 2.57 & 0.39 \\ - & 2.27 & 0.41 \\ - & - & 1.0 \end{pmatrix} (Depth = 0.94\, mm)$$

(b)

Figure 22. (a)Stress tensor values for the SZ of the 400/100 condition. (b) Stress tensor values for the TMAZ of the 400/100 condition. All stresses given in MPa. Tensors are symmetric.

In addition to the stress with depth measurements, measurements taken across the root of the weld revealed a different profile than those taken across the crown of the plate (Figure 23). Profiles displayed the characteristic "M" shape, and decreasing heat input

generally resulted in larger residual stresses. However, more asymmetry was observed between stress peaks on the advancing and retreating sides. The 500/25 and 400/100 conditions have longitudinal stresses of 621 MPa and 402 MPa, respectively while stress peaks on the retreating side are nearly 140 MPa lower. Less asymmetry was observed for the 400/50 condition, where peaks on the advancing and retreating sides were separated by 70 MPa.

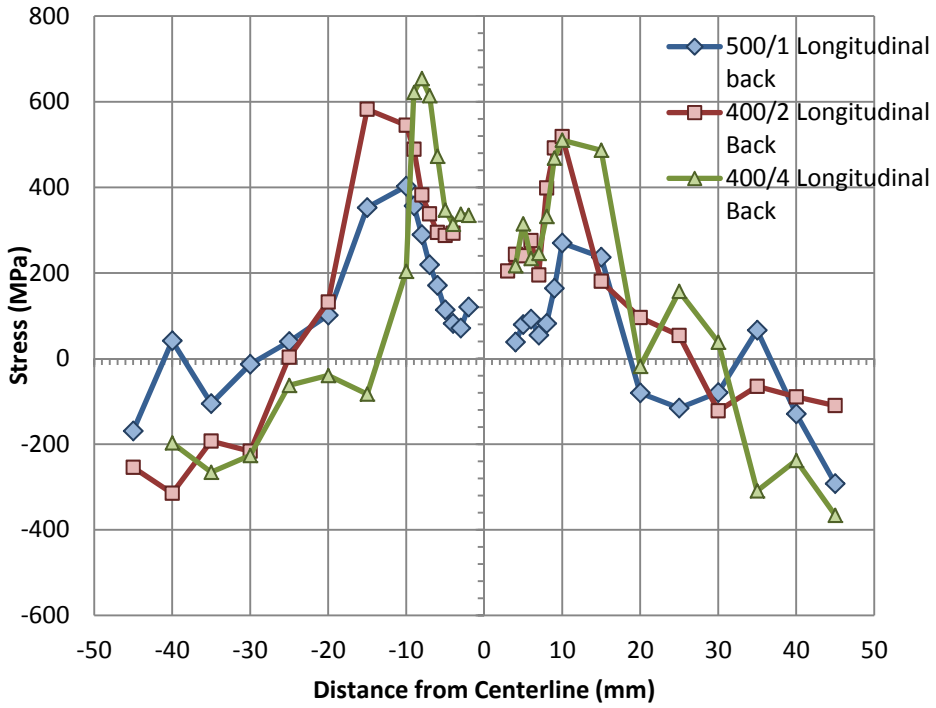

Figure 23. Residual stress profiles from the root of the weld on Plate 1

THIS PAGE INTENTIONALLY LEFT BLANK

IV. DISCUSSION

There are several important points to address when discussing residual stress plots across friction stir welds in any material: the shape and characteristics of the stress profile; the percentage of yield for peak stress values; the effects of all components in the stress tensor; and the implications all these have on material performance.

A. RESIDUAL STRESS PROFILES

As hypothesized in the introduction, the magnitude of measured residual stresses on MA956 increase as the heat index of the weld is lowered. Not only do the maximum values immediately adjacent to the tool shoulder increase, but the stresses across the stir zone increase as well. This observation was the same on both the crown and root sides of the welded plate. This trend shows that friction stir welded ODS steels follow the same pattern as observed in other steels that decreasing heat index, or increasing weld pitch, will increase the magnitude of residual stress across the weld profile.

While the measurements in this thesis agree qualitatively with the similar work of Mathon on PM2000, there are subtle differences in peak asymmetry, profile width, and stress across the stir zone. The first difference between stress profiles for MA956 and those measured for PM2000 was the lack of asymmetry in the maximum longitudinal stress values on the crown side of the weld. Peak asymmetry was observed for the 400/100 and 500/25 conditions on the root of the weld, but no distinction is made between crown and root for Mathon's work which used neutron diffraction. Mathon describes a difference of 130 MPa between the advancing and retreating sides of the weld, with the advancing side being higher. This asymmetry was not observed in measurements of the crown of Plate 1 and Plate 2. Values on the advancing and retreating side of the 500/25 condition and 400/100 condition varied only 16 MPa and 27 MPa, respectively. Differences of that magnitude are not sufficient to conclude that asymmetry exists. However, for the 400/50 condition, the difference between advancing and retreating longitudinal stress maxima was 85 MPa, with the larger peak on the advancing side. This may be due to the difference in relative velocity between the tool and the plate

for the advancing and retreating sides as suggested by Mathon [20]. A possible explanation is that the residual stress in ODS steels does not scale entirely linearly with a decreased heat index. Above and below certain values for weld pitch the differences between advancing and retreating sides may not be significant enough to cause a change in the residual stress values. At intermediate values for weld pitch, the combination of microstructural evolution and heat input due to friction may lead to significantly different values for residual stress. It is also important to note the differences in the experimental conditions between results presented here and work by Mathon. The PM2000 plate was only 1.3 mm thick and the tool was half the size of the tool used in this work, making direct comparison between experiments difficult. The clamping force was 14 kN versus the 17.8 kN used on the MA 956 plate, and Mathon's weld was performed at 600 rpm and 50 mmpm [20].

For every condition measured here, the longitudinal residual stresses were a significant percentage of the yield strength in the FSW affected material. For the lowest heat index on Plate 1, the 400/100 condition, longitudinal residual stresses were approximately $0.9\sigma_y$ (Figure 24). Even the peak longitudinal stress at the highest HI condition, which was expected to have the lowest residual stresses, approached $0.6\sigma_y$. This trend of increasing maximum stresses is also found in Plate 2, where peak stresses were only 4 MPa below the 909 MPa yield strength of the base metal as measured by Baker [5]. The residual stress profile was normalized by the yield strength. The yield strengths used were measured by Baker for the same FSW conditions. The yield strength of the weld material varied across the weld and was accounted for using microhardness traces across the weld [5]. Based on these hardness measurements, material beyond 10 mm from the weld centerline had the same hardness/yield strength as the base metal, 909 MPa. Material inside 10 mm of the weld centerline had a yield strength of 539 MPa. A transition region occurs in the TMAZ, but not enough tensile data is available to differentiate between the TMAZ and the BM. Asymmetry appears for the 400/100 condition in Figure 24, however it occurs based on the distinction between the base metal yield strength and stir zone yield strength and not asymmetry in stress values.

The data gathered here fits nicely with work done by Mathon. In FSW of PM2000, maximum longitudinal residual stresses reached $0.5\sigma_y$, when compared to a yield strength of 900 MPa in the base metal. While Mathon compares the residual stress maxima on the advancing side to the base metal, more detailed data is available on the local yield strength from work by Baker [5]. He shows that the actual yield strength across the base metal decreases to 530 MPa for the 500/25 condition. This suggests that residual stresses measured here are actually a much larger fraction of yield than initially thought. These values are consistent with other work on more traditional steels that show residual stresses in steels are around 80% of yield strength, and are a much higher fraction of yield strength than those measured in aluminum which generally are 4050% of yield strength [18, 19].

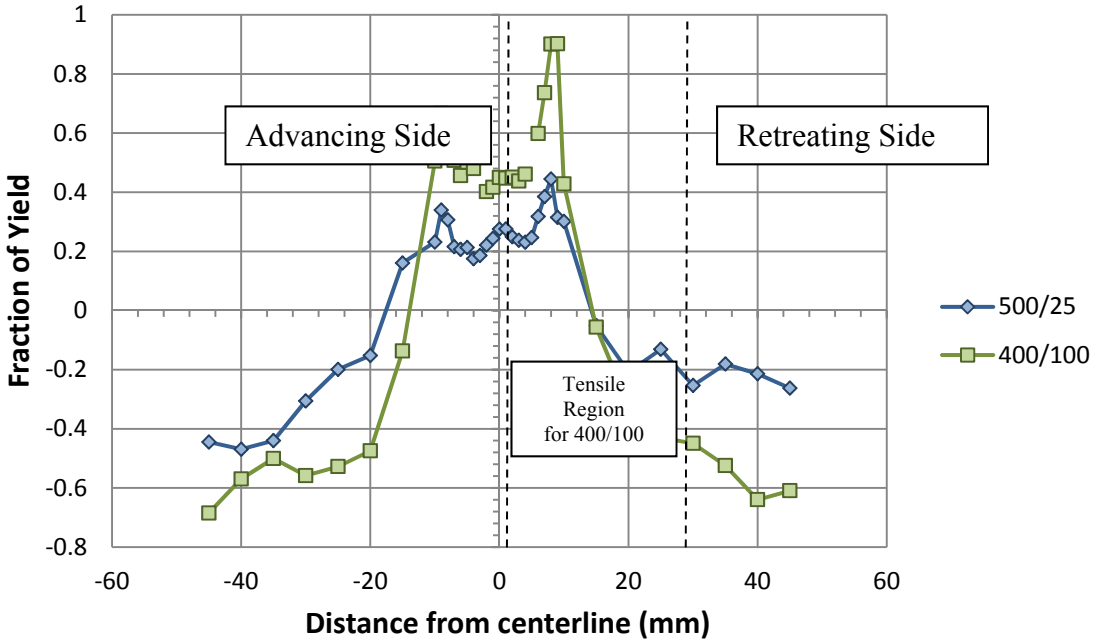

Figure 24. Normalized Longitudinal stresses from the crown of Plate 1. Data within 10 mm of the weld centerline was normalized to a yield strength of 530 MPa or 539 MPa (500/25 and 400/100, respectively), while data beyond these points were normalized to the BM yield of 909 MPa.

Lowering heat input the weld not only changed the maximum longitudinal residual stress values, it also affected the width of the tensile region. Based on modeling

work done by Bastier on aluminum alloys, increasing the traverse speed for the same rotational speed should produce a narrower tensile region, with peak longitudinal stresses closer together (Figure 24) [17]. Larger heat inputs can result by changing either of the two main welding parameters, rotational speed of the tool and traverse speed. More heat is generated due to friction and plastic deformation at the tool interface due to an increased rotational speed. Decreasing traverse speeds also increases heat generation in the weld as the tool has more time to develop heat at the tool plate interface. A colder weld with a lower rotational speed or a higher traverse speed should have a sharpened profile with a smaller heat affected zone. The trend was observed in both Plate 1 and Plate 2, where the tensile region was narrower in the 400/50 condition than it was in the 400/100 condition. However, the trend was not observed between the 500/25 and 400/50 conditions. The 400/50 tensile region was significantly wider than that for the 500/25 condition, but a comparison between these conditions cannot be made as both the welding speed and rotational speeds were changed. The results that are comparable show that for fixed tool rotational speed, decreasing traverse speed will widen the residual stress profile.

Also of interest is the magnitude of stresses across the 'trough' of the residual stress profile, the area that corresponds to the weld nugget, or stir zone. This region is approximately 10 mm on either side of the weld centerline. As with peak stresses just outside the weld nugget, stresses in the trough also increase with a decrease in heat input. This is likely due to higher thermal gradients for materials with a lower heat input, as well as reduced softening across the stir zone. As the material is softened, the yield strength of the material decreases and it is not able to support the peak stresses seen in the TMAZ. Upon cooling, coarser grains do not possess the necessary strength to support large residual stresses. However, the TMAZ may support higher residual stresses as it is the region that encounters the highest thermal gradients and still retains the smaller grain size of the base metal. Baker shows that even up to the weld shoulder, hardness values and grain size are equivalent with those in the base material [5].

Longitudinal stresses long the weld centerline remained constant with depth while the longitudinal stresses decreased with depth in the TMAZ. Along the centerline, out of

plane components were small in comparison to longitudinal and transverse components and did not change significantly with depth. This indicates that there is no stress gradient at the surface of the stir zone. However, a significant gradient was observed in the TMAZ. It was initially postulated that the stress decreased with depth due to the availability of material constraints, which would give a more three-dimensional stress tensor with larger stresses normal to the plate. Analysis of the stress tensors from various depths supports this, as σ_{13}, σ_{12} and σ_{22} increase with depth. However, it is possible that the change in stress with depth is a result of the conical profile of the stir zone and not simple additional material constraint. As material is removed, the position of the stress measurement with respect to the tool shoulder changes (Figure 3). Stress measurements taken at depth may actually be in the HAZ and not the TMAZ. Three dimensional mapping of the residual stresses in FSW of Al 2024-T3 has shown that stress gradients are fairly steep, especially on the advancing side of the weld [24]. However, across the root of the weld, stress profiles in 2024-T3 showed lower residual stress peaks than those across the crown whereas in Plate 1, stresses were roughly comparable or even higher (Figure 23). More research needs to be conducted to determine the stress profiles of plate cross sections.

B. IMPLICATIONS

Tensile longitudinal stresses left untreated can be very detrimental to the fatigue life of affected parts. The extent to which residual stresses will reduce the fatigue strength for a given fatigue life can be estimated through the use of the Goodman relationship, which shows the drastic reduction of the factor of safety in fatigue loaded parts (Figure 25).

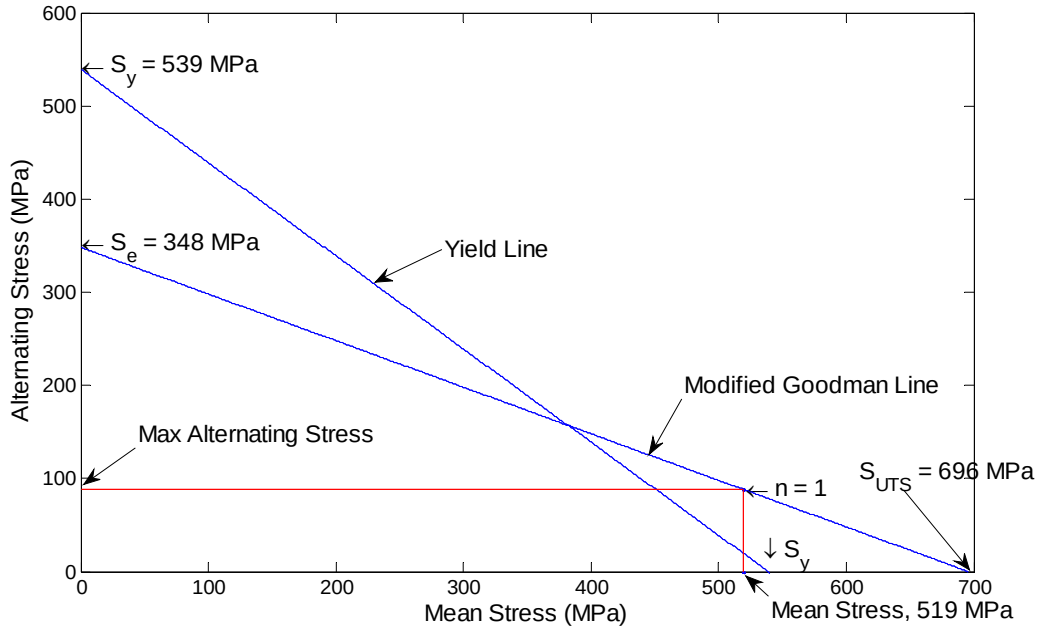

Figure 25. A Modified-Goodman plot for the stir zone of the 400/100 condition. The measured residual stresses are near the yield strength of the SZ. In this example, for a safety factor of 1 (failure), an alternating load of only 89 MPa need be applied.

On this plot, the mean stress is the addition of and residual stresses and constant applied loads. The full stress tensor is available for the residual stresses, so the Von Mises stress may be calculated from the following relationship [25]:

$$\sigma_v = \sqrt{\sigma_{11}^2 - \sigma_{11}\sigma_{22} + \sigma_{22}^2 + 3\tau_{12}^2} \tag{9}$$

A part undergoing FSW at the 400/100 condition would have a mean Von Mises stress of 519 MPa in the stir zone.

Creating a Modified Goodman plot for this condition requires the knowledge of specific material properties. For material in the stir zone of this condition σ_y = 539 MPa, and σ_{UTS} = 696 MPa. The fatigue strength for MA956 is not known, so the endurance limit σ_e was estimated to be half σ_{UTS}, which is a less conservative assumption. Generally σ_e is calculated from the formula [25]:

$$\sigma_e = k_a k_b k_c k_d k_e k_f (0.5\sigma_{UTS}) \tag{10}$$

where $k_a - k_f$ are surface factors, geometry factors, loading factors etc. As an engineering first assumption, these factors were assumed to be unity. Taking each of these into consideration would ultimately lower the value for σ_e. The factor of safety, or the maximum alternating load, may be calculated from the Modified Goodman equation [25]:

$$\frac{\sigma_a'}{\sigma_e} + \frac{\sigma_m'}{\sigma_{UTS}} = \frac{1}{n} \tag{11}$$

In this case, the maximum alternating load was calculated to be 88.5 MPa for n = 1. In practice, a safety factor should be much greater than this, especially in the likely applications for MA956.

In other analyses, the longitudinal stresses alone will play the most significant role, as opposed the Von Mises equivalent stress. In piping application, FSW processes will be performed circumferentially to join segments. In this case, the limiting stress will most likely be longitudinal residual stress, which as defined here is in the same direction as the hoop stress, σ_θ.

The goal of these experiments was to determine how the residual stress changes as a function of heat input. This data shows that as heat input to the weld decreases, the magnitude of tensile residual stresses increases. While the research is by no means exhaustive, it can give insight into the optimization of FSW parameters. While higher heat inputs were shown to produce the lowest residual stresses, there are other trade-offs that come with this benefit. Higher heat input also coarsens grains significantly more than colder welds, and there is a resultant drop in yield strength [5]. Welding Engineers will have to balance concern for residual stress levels with a possibly unsafe drop in yield strength across the weld nugget. High residual stresses or large losses in yield strength can be avoided, but not simultaneously. Optimization for FSW of ODS steels like MA956 will likely result in a mid-range heat input solution in an attempt to retain the attractive properties of the MA956 base metal. Other options include post weld heat treatments or peening processes to reduce residual stresses.

THIS PAGE INTENTIONALLY LEFT BLANK

V. CONCLUSIONS

This thesis characterized the residual stresses generated by friction stir welding plates of MA956 as a function of changing heat input.

- **Install and test a new x-ray residual stress instrument at NPS.** The x-ray diffractometer from Proto Manufacturing was setup and tested using stress free steel powder and high stress steel standards. The system consistently gave accurate readings for residual stresses on these standard materials.
- **Measure residual stress distributions around friction stir welds in ODS steel MA956.** All residual stress distributions displayed the characteristic "M" profile across the weld. Peak tensile residual stresses occurred just beyond the tool shoulder, with reduced tensile stresses in the stir zone. Asymmetry between peak longitudinal stresses on the advancing versus retreating sides in the crown of the weld only occurred in the 400/50 condition, with larger stresses unexpectedly on the retreating side. Asymmetry in tensile peak values occurred for the 500/25 and 400/100 in the root of the weld. In each case, longitudinal residual stresses were larger than transverse stresses, which were larger than all out of plane components.
- **Determine the relationship between heat input (HI) to welds and the magnitude of resulting residual stresses.** As predicted from previous research on FSW, lowering the HI by decreasing the rotational speed or increasing the traverse speed increased the magnitudes of residual stresses across the weld profile. Residual stresses exceeding 90% of yield strength were observed for the lowest heat input conditions, which may significantly shorten fatigue life. Optimization of FSW parameters will likely require a balance in heat input in order to simultaneously minimize loss in yield strength and increase in residual stresses.

THIS PAGE INTENTIONALLY LEFT BLANK

LIST OF REFERENCES

[1] S. Zinkle and N. Ghoniem, "Operating temperature windows for fusion reactor structural materials," *Fusion Eng. Des.,* vol. 51–52, pp. 5571, Nov 2000.

[2] S. J. Zinkle and J. T. Busby, "Structural materials for fission and fusion energy," *Materials Today,* vol. 12, pp. 12–19, 2009.

[3] A. Kimura, "Current status of reduced-activation ferritic/martensitic steels R&D for fusion energy," *Mater. Trans.,* vol. 46, pp. 394404, Mar. 2005.

[4] P. J. Maziasz and et al., "New ODS ferritic alloys with dramatically improved high-temperature strength," *J. Nucl. Mater.,* 1999.

[5] B. W. Baker, L. N. Brewer, et al., "Influence of heat input on friction stir welding for the ODS Steel MA956," in *Friction Stir Welding and Processing VII*, R. S. Mishra, M. W. Mahoney, S. Yutaka, Y. Hovanski, and R. Verma, Eds. Wiley, 2013.

[6] D. T. Hoelzer and J. Bentley, M. A., "Influence of particle dispersions on the high-temperature strength of ferritic alloys," *J. Nucl. Mater.,* vol. 367, pp. 166–172, Aug. 1, 2007.

[7] R. Klueh and P. Maziasz, "Tensile and creep properties of an oxide dispersion-strengthened ferritic steel," *J. Nucl. Mater.,* vol. 307, pp. 773777, Dec. 2002.

[8] M. McKimpson and D. O'Donnell, "Joining Ods Materials for High-Temperature Applications," *JOM-J. Miner. Met. Mater. Soc.,* vol. 46, pp. 4951, Jul. 1994.

[9] R. Lindau and M. Klimenkov,"Mechanical and microstructural characterization of electron beam welded reduced activation oxide dispersion strengthened - Eurofer steel," *J. Nucl. Mater.,* vol. 416, pp. 2229, Sep 1, 2011.

[10] H. J. K. Lemmen and K. J. Sudmeijer, I, "Laser beam welding of an Oxide Dispersion Strengthened super alloy," *J. Mater. Sci.,* vol. 42, pp. 52865295, Jul. 2007.

[11] P. Miao and G. R. Odette, "The microstructure and strength properties of MA957 nanostructured ferritic alloy joints produced by friction stir and electro-spark deposition welding," *J. Nucl. Mater,* vol. 367, pp. 11971202, Aug 1, 2007.

[12] W. T. Han and F. R. Wan, "Grain characteristic and texture evolution in friction stir welds of nanostructured oxide dispersion strengthened ferritic steel," *Sci. Technol. Weld. Join,* vol. 16, pp. 690696, Nov. 2011.

[13] R. S. Mishra and Z. Y. Ma, "Friction stir welding and processing," *Materials Science & Engineering R-Reports,* vol. 50, pp. 178, Aug 31 2005.

[14] R. Nandan, T. DebRoy, and H. K. D. H. Bhadeshia, "Recent advances in friction-stir welding - Process, weldment structure and properties," *Prog. Mater. Sci.,* vol. 53, pp. 9801023, Aug. 2008.

[15] M. Peel and A. Steuwer, "Microstructure, mechanical properties and residual stresses as a function of welding speed in aluminum AA5083 friction stir welds," *Acta Mater.,* vol. 51, pp. 47914801, Sep 15, 2003.

[16] C. M. Chen and R. Kovacevic, "Parametric finite element analysis of stress evolution during friction stir welding," *Proc. Inst. Mech. Eng. Part B-J. Eng. Manuf.,* vol. 220, pp. 13591371, Aug. 2006.

[17] A. Bastier and M. H. Maitournam, "Modeling of the residual state of friction stir welded plates," *J. Mater. Process. Technol.,* vol. 200, pp. 2537, May 8, 2008.

[18] A. Steuwer and S. J. Barnes, "Friction Stir Welding of HSLA-65 Steel: Part II. The Influence of Weld Speed and Tool Material on the Residual Stress Distribution and Tool Wear," *Metall. Mater. Trans. A-Phys. Metall. Mater. Sci.,* vol. 43A, pp. 23562365, Jul. 2012.

[19] A. Reynolds and W. Tang, "Structure, properties, and residual stress of 304L stainless steel friction stir welds," *Scr. Mater.,* vol. 48, pp. 12891294, May. 2003.

[20] M. H. Mathon and V. Klosek, "Study of PM2000 microstructure evolution following FSW process," *J. Nucl. Mater.,* vol. 386–88, pp. 475478, Apr 30, 2009.

[21] B. D. Cullity, *Elements of X-Ray Diffraction.* Reading, Mass.: Addison-Wesley, 1986.

[22] B. J. Banazwski, L. N. Brewer, and S. K. Menon, "Using x-ray diffraction to asses residual stresses in laser peened and welded aluminum," M.S. thesis, Mech. Eng. Dept., Naval Postgraduate School, Monterey., CA, 2011.

[23] I. C. Noyan and J. B. Cohen, *Residual Stress: Measurement by Diffraction and Interpretation.* Berlin, Germany: Springer-Verlag, 1987.

[24] M. Sutton, A. Reynolds, D. Wang, and C. Hubbard, "A study of residual stresses and microstructure in 2024-T3 aluminum friction stir butt welds," *J. Eng. Mater. Technol. -Trans. ASME,* vol. 124, pp. 215221, Apr. 2002.

[25] R. Budynas and K. Nisbett, *Shigley's Mechanical Engineering Design.* New York: McGraw Hill, 2011.

INITIAL DISTRIBUTION LIST

1. Defense Technical Information Center
   Ft. Belvoir, Virginia

2. Dudley Knox Library
   Naval Postgraduate School
   Monterey, California